

Spin-orbit-entangled electronic phases in 4d and 5d transition-metal compounds

Tomohiro Takayama,^{1,2} Jiří Chaloupka,^{3,4} Andrew Smerald,¹ Giniyat Khaliullin,¹ and Hidenori Takagi^{1,2,5}

¹Max Planck Institute for Solid State Research, Heisenbergstrasse 1, 70569 Stuttgart, Germany

²Institute for Functional Matter and Quantum Technologies,
University of Stuttgart, Pfaffenwaldring 57, 70550 Stuttgart, Germany

³Department of Condensed Matter Physics, Masaryk University, Brno, Czech Republic

⁴Central European Institute of Technology, Masaryk University, Brno, Czech Republic

⁵Department of Physics, University of Tokyo, 7-3-1 Hongo, Tokyo 113-0033, Japan

(Dated: February 5, 2021)

Complex oxides with 4d and 5d transition-metal ions recently emerged as a new paradigm in correlated electron physics, due to the interplay between spin-orbit coupling and electron interactions. For 4d and 5d ions, the spin-orbit coupling, ζ , can be as large as 0.2-0.4 eV, which is comparable with and often exceeds other relevant parameters such as Hund's coupling J_H , noncubic crystal field splitting Δ , and the electron hopping amplitude t . This gives rise to a variety of spin-orbit-entangled degrees of freedom and, crucially, non-trivial interactions between them that depend on the d -electron configuration, the chemical bonding, and the lattice geometry. Exotic electronic phases often emerge, including spin-orbit assisted Mott insulators, quantum spin liquids, excitonic magnetism, multipolar orderings and correlated topological semimetals. This paper provides a selective overview of some of the most interesting spin-orbit-entangled phases that arise in 4d and 5d transition-metal compounds.

I. INTRODUCTION

In the 1960's and 70's, correlated-electron physics in transition-metal oxides was already an active field of research, and a major topic in condensed matter science. The basic picture of spin and orbital ordering and the interplay between them was unveiled during this period, and collected into the Kanamori-Goodenough rules. However, the exploration of exotic electronic phases beyond conventional magnetic ordering was stymied by a lack of materials and theoretical tools.

In 1986, high- T_c superconductivity was discovered in the layered 3d Cu oxides, which accelerated both experimentally and theoretically the search for novel spin-charge-orbital coupled phenomena produced by electron correlations. The major arena of such exploration was complex oxides with 3d transition metal ions from Ti to Cu, which led to the discoveries of unconventional superconductivity, colossal magneto-resistance, multiferroics and exotic spin-charge-orbital orderings. 4d and 5d transition metal oxides were also studied, but not as extensively as 3d transition metal oxides, except for 4d Sr_2RuO_4 , where possible p -wave superconductivity was discussed. This was at least partially due to the less prominent effect of correlations in 4d and 5d, which arises from the wavefunctions being more spatially extended than in 3d.

In the late 2000's, the layered perovskite Sr_2IrO_4 was identified as a weak Mott insulator, and the crucial role of spin-orbit coupling (SOC) in stabilizing the Mott state awoke a growing interest in 5d Ir oxides and other 4d and 5d compounds. For Ir^{4+} ions, there are five 5d-electrons, which reside in the t_{2g} manifold, and therefore have an effective orbital moment $L = 1$ and form a spin-orbit-entangled $J = 1/2$ pseudospin. These $J = 1/2$ pseudospins behave in some ways like $S = 1/2$ spins, but have

an internal spin-orbital texture where the up/down spin states reside on different orbitals. The resulting spin-orbital entanglement gives rise to non-trivial interactions between the $J = 1/2$ pseudospins, and this led to the proposal that the Kitaev model, with bond-dependent Ising interactions, can be realized on edge-shared honeycomb networks of $J = 1/2$ pseudospins. In consequence, $J = 1/2$ honeycomb magnets made out of 5d⁵ Ir^{4+} and 4d⁵ Ru^{3+} ions have been extensively studied over the last ten years, in an effort to discover the expected quantum spin-liquid state and associated Majorana fermions.

Despite the considerable excitement, the d⁵ $J = 1/2$ Mott state is not the only spin-orbit-entangled state of interest among the many 4d and 5d transition metal compounds. With different filling of d -orbitals and different local structures, a rich variety of spin-orbit-entangled states can be formed, which are characterized not only by dipolar moments but also by multipoles such as quadrupolar and octupolar moments. Exotic states of such spin-orbit-entangled matter can be anticipated, reflecting the internal spin-orbital texture and the lattice symmetry, and including excitonic magnetism and multipolar liquids.

4d and 5d transition metal compounds also form interesting itinerant states of matter, with one prominent example being the topological semimetal. This arises from the interplay of lattice symmetry and SOC, and, in contrast to typical topological semimetals, 4d and 5d semimetals tend to also have strong electron correlations. Thus they provide an arena in which to study the overlap between topological physics and strong correlation.

Spin-orbit-entangled phases are also formed in 4f and 5f electron systems, which have been extensively studied, and it is worth spelling out what makes 4d and 5d electron systems distinct. One obvious difference is that they interact through exchange processes with a much larger

energy scale, making them more accessible to experiment, and thus increasing the variety of phenomena that can be effectively probed. Also, the spin-orbit-entangled J states in $4d$ and $5d$ systems are much less localized than those of $4f$, and can often be itinerant, opening up, for example, the exploration of correlated topological semimetals, and SOC driven exotic states formed near metal-insulator transitions. The d - and the f - electron systems thus clearly play a complementary role in the exploration of spin-orbit-entangled phases.

This review is intended to provide readers with a broad perspective on the emerging plethora of $4d$ and $5d$ transition metal oxides and related compounds. We would like to address two basic questions: 1) What kind of exotic phases of spin-orbit-entangled matter are expected in $4d$ and $5d$ compounds? 2) To what extent are the proposed concepts realized? We limit our discussion to the compounds with octahedrally coordinated $4d$ and $5d$ transition metal ions accommodating less than 6 electrons in their t_{2g} orbitals (low-spin configuration), where the effect of the large SOC is prominent due to the smaller crystal field splitting of t_{2g} orbitals as compared to e_g . As there are many reviews of pseudospin-1/2 d^5 Mott insulators, here we will discuss spin-orbit-entangled states in $4d$ and $5d$ transition metal compounds from a broader perspective, covering, in addition to d^5 compounds, d^1 , d^2 and d^4 insulators, as well as itinerant systems with strong SOC.

II. CONCEPT OF SPIN-ORBIT-ENTANGLED STATES AND MATERIALS OVERVIEW

In Mott insulators, charge fluctuations are frozen, and the low-energy physics is driven by the spin and orbital degrees of freedom of the constituent ions. In $3d$ compounds, orbital degeneracy and hence orbital magnetism is largely quenched by noncubic crystal fields and the Jahn-Teller (JT) mechanism, and magnetic moments are predominantly of spin origin (with some exceptions mentioned below). The large SOC in $4d$ and $5d$ transition metal ions competes with and may dominate over crystal field splitting and JT effects, and the revived orbital magnetism becomes a source of unusual interactions and exotic phases. We first discuss the spin-orbital structure of the low-energy states of transition metal ions in a most common, cubic crystal field environment, and then proceed to their interactions and collective behavior.

A. Spin, orbital, and pseudospin moments in Mott insulators

The valence wavefunctions of $4d$ and $5d$ ions are spatially extended and the Hund's coupling is smaller than the cubic crystal field splitting, $10Dq$, between t_{2g} and e_g orbitals. Low-spin ground states are therefore stabilized for $4d$ and $5d$ electron configurations more fre-

quently than in the $3d$ case, where the Hund's coupling typically overcomes the t_{2g} - e_g crystal field splitting. In the low-spin state, electrons occupy t_{2g} orbitals forming total spin-1/2 (d^1 , d^5), spin-1 (d^2 , d^4), and spin-3/2 (d^3). In all of them (except d^3 orbital singlet not discussed here), the orbital sector is threefold degenerate, formally isomorphic to the p -orbital degeneracy, and can thus be described in terms of an effective orbital angular momentum $L = 1$. (The effective orbital angular momentum is often distinguished by a special mark, see, e.g., the "fictitious angular momentum" \tilde{l} in the textbook by Abragam and Bleaney,¹ but here we conveniently choose a simpler notation L .) By a direct calculation of matrix elements of the physical orbital momentum $L_d = 2$ of d -electrons within the t_{2g} manifold, one finds a relation $\mathbf{L}_d = -\mathbf{L}$ between the angular momentum operators.

By employing the effective \mathbf{L} operator, the SOC reads as $H = \mp\lambda\mathbf{S}\mathbf{L}$, where the negative (positive) sign refers to a less (more) than half-filled t_{2g} shell of d^1 , d^2 (d^4 , d^5) configurations, and λ is related to the single-electron SOC strength, ζ , via $\lambda = \zeta/2S$. The resulting spin-orbital levels are shown in Fig. 1(a). Apparently, SOC breaks particle-hole symmetry: due to the above sign change, the levels are mutually inverted within the pairs of complementary electron/hole configurations such as d^1/d^5 and d^2/d^4 . The ground states thus have completely different total angular momentum $\mathbf{J} = \mathbf{S} + \mathbf{L}$. Its constituents \mathbf{S} and \mathbf{L} align in parallel (antiparallel) fashion for the less (more) than half-filled case. The corresponding "shapes" of the ground-state electron densities are depicted in Fig. 1(b). Their nonuniform spin polarization with a coherent mixture of spin-up and down densities clearly shows the coupling between the spin and the orbital motion of electrons.

The observed variety of ionic ground states among d^n configurations brings about a distinct physics for each of the d^n ions. d^1 and d^2 ions with $J > 1/2$ host higher order magnetic multipoles, and may lead to unconventional high-rank order parameters "hidden" magnetically. Nominally nonmagnetic $J = 0$ d^4 ions may develop unusual magnetism due to condensation of the excited $J = 1$ level. d^5 ions with Kramers doublet $J = 1/2$ are formally akin to spin one-half quantum magnets which are of special interest in the context of various quantum ground states.

When evaluating the magnetic properties, the orbital component of the magnetic moment needs to be incorporated. In terms of the effective \mathbf{L} , the magnetic moment operator reads as $\mathbf{M} = 2\mathbf{S} - \mathbf{L}$. In principle, \mathbf{L} comes with the so-called covalency factor κ but we omit it for simplicity. For d^1 with parallel $L = 1$ and $S = 1/2$, one has $L = 2S$ and thus $M = 0$, i.e. the $J = 3/2$ quartet has zero g -factor and is thus nonmagnetic. In reality, $\kappa < 1$ makes the compensation only partial, resulting in a small magnetic moment. For d^2 with $S = L = J/2$, one finds $\mathbf{M} = (1/2)\mathbf{J}$, i.e. $g = 1/2$. d^4 with $J = 0$ is a nonmagnetic singlet. d^5 with antiparallel $S = 1/2$ and $L = 1$ has g -factor $g = -2$, i.e. it is of opposite sign relative to

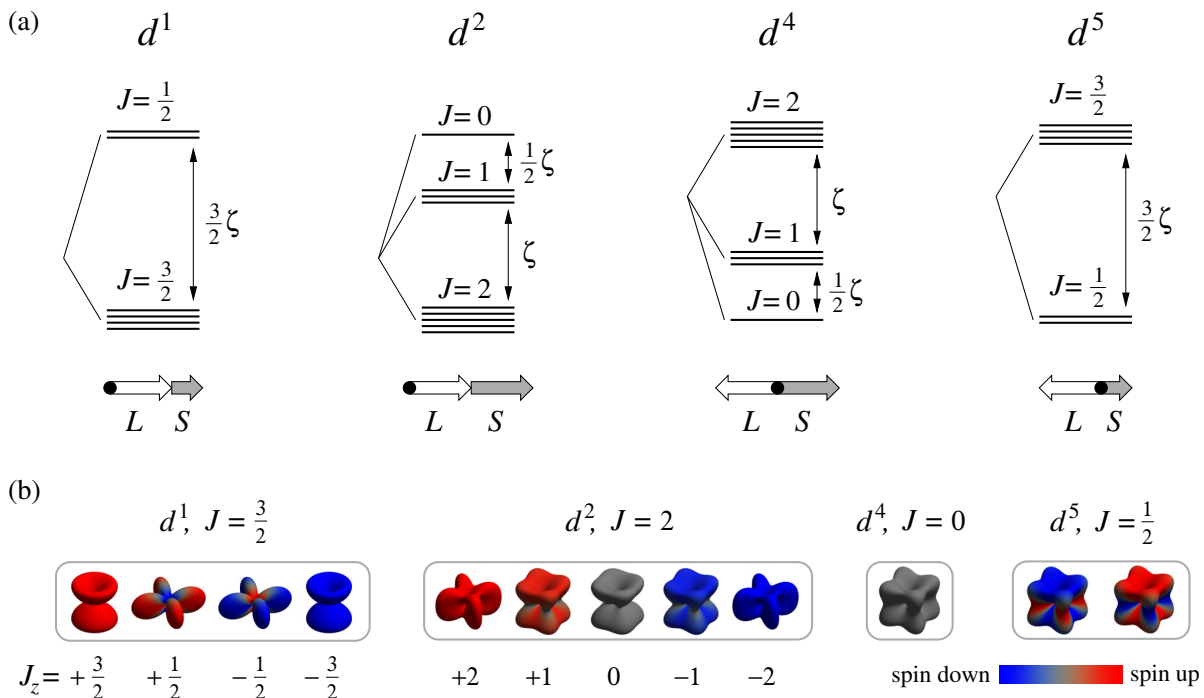


FIG. 1. (a) Low-energy levels of d^1 , d^2 , d^4 , and d^5 ions in cubic crystal field. The degeneracy of the levels is shown by the number of close lines. For less than half-filled t_{2g} shell, the SOC aligns the effective orbital angular momentum L and spin S to form larger total angular momentum: $J = 3/2$ quartet in d^1 case and $J = 2$ quintuplet in d^2 case, respectively. In the case of more than half-filled t_{2g} shell, L and S are antialigned, leading to $J = 0$ singlet ground state for the d^4 configuration while the d^5 one hosts pseudospin $J = 1/2$. (b) Orbital shapes corresponding to the ground-state J -levels. Only the angular distribution of the electron density is considered. It is represented by a surface plot where the distance to the origin is proportional to the integral density in the corresponding direction. The color of the surface indicates normalized spin polarization $(\rho_{\uparrow} - \rho_{\downarrow})/(\rho_{\uparrow} + \rho_{\downarrow})$ taking values in the range $[-1, +1]$. It is shown for electrons in the case of d^1 and d^2 states and for the holes in the t_{2g}^6 configuration in the case of d^4 and d^5 states.

the electron g -factor. The above g -factors strongly deviating from pure spin $g = 2$ are the fingerprints of large orbital contribution to magnetism. In the d^5 case, e.g., one finds that $\mathbf{S} = (-1/3)\mathbf{J}$ only, while $\mathbf{L} = (4/3)\mathbf{J}$; that is, magnetism of d^5 compounds is predominantly of orbital origin.

Figure 2 focuses in detail on the particular case of the d^2 configuration. The $J = 2$ ground state is special because it is isomorphic to a d -electron with orbital moment $L_d = 2$, and thus it has to split under cubic crystal field into a triplet of T_{2g} and a doublet of E_g symmetries (often denoted as Γ_5 and Γ_3 states, respectively). The corresponding wavefunctions in the basis of J_z eigenstates $|J_z\rangle$ are: $|\pm 1\rangle$, and $(|+2\rangle - |-2\rangle)/\sqrt{2}$ for T_{2g} , and $|0\rangle$ and $(|+2\rangle + |-2\rangle)/\sqrt{2}$ for E_g states, just like for single electron d -orbitals of t_{2g} and e_g symmetries, as required by the above isomorphism. Physically, this splitting arises, e.g., due to the admixture of the $t_{2g}^1 e_g^1$ configuration into t_{2g}^2 by SOC. More specifically, second-order energy corrections to T_{2g} and E_g levels are different, which gives a splitting of the $J = 2$ level by $\sim \zeta^2/10Dq$. With SOC parameter $\zeta = 0.2$ eV and $10Dq = 3$ eV, typical for $4d$ and $5d$ ions, one obtains a sizable splitting of 20 meV,

with the E_g doublet being the lower one. It is evident from the above wavefunctions that the E_g state has no dipolar moment and is therefore magnetically silent. Instead, the E_g doublet hosts quadrupolar and octupolar moments. This is again analogous to e_g electrons, which are quadrupole active, and it has been discussed in the context of manganites that they may host an octupolar moment as well.²⁻⁴ While this effect was not observed in real e_g orbital systems, the spin-orbit-entangled E_g doublet may show octupolar order driven by intersite exchange interactions, unless JT coupling to lattice stabilizes quadrupolar order instead.

Concerning the JT activity of the ionic ground states, the d^4 singlet and d^5 Kramers doublet possess no orbital degeneracy and are thus “JT-silent” in the first approximation. However, both d^1 and d^2 are JT active ions, and structural phase transitions as in usual $3d$ systems can be expected. As shown in Fig. 1(b), the shapes of the $\pm 3/2$ and $\pm 1/2$ states of the d^1 ion are different; therefore, they will split under tetragonal lattice distortions. In fact, these two Kramers doublets can be regarded as an effective e_g orbital, so JT coupling would read exactly as for the e_g orbital, albeit with an effective JT

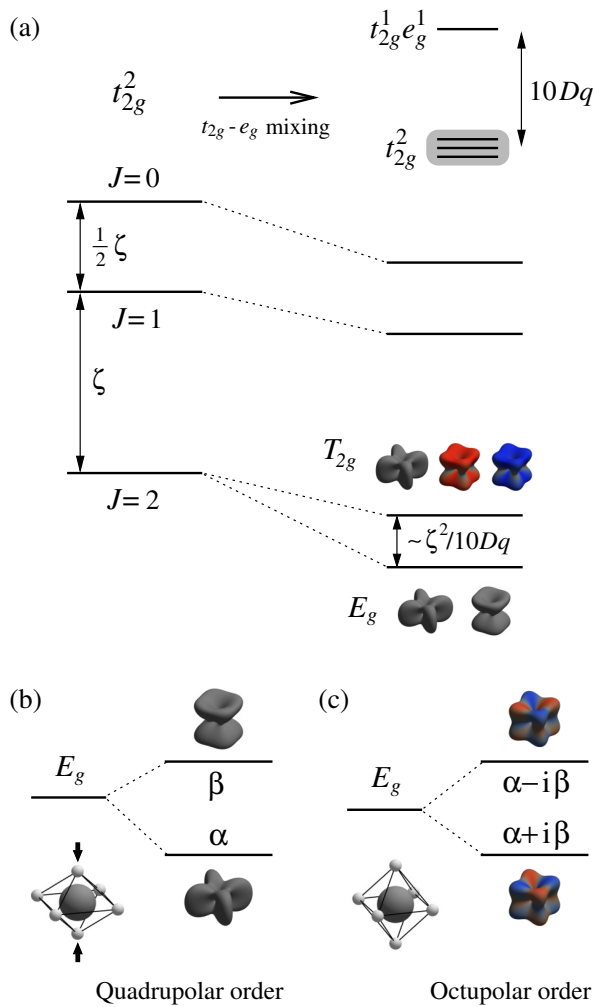


FIG. 2. (a) Shifts and splitting of the $J = 0, 1, 2$ levels of d^2 ion when considering mixing of the ground state t_{2g}^2 configuration with $t_{2g}^1 e_g^1$ states by virtue of SOC. Focusing on the lowest levels, we find the originally five-fold degenerate $J = 2$ states split into an E_g doublet and T_{2g} triplet. Evaluated perturbatively for $\zeta \ll 10Dq$, the splitting comes out proportional to $\zeta^2/10Dq$. (b) Tetragonal compression leads to an increased repulsion of d -electrons from apical oxygen ions and further singles out “planar” states from E_g and T_{2g} sets. The quadrupolar moment hosted by the E_g doublet gets pinned this way. (c) Complex combinations of the E_g doublet states that expose the octupolar moment of “cubic” shape.

coupling constant reduced by $1/\sqrt{3}$, as a result of SOC unification of the Hilbert space. Similarly, the E_g doublet of the $J = 2$ manifold in the case of a d^2 ion should experience JT coupling. Overall, the JT effect (and related structural transition) is still operative, but it affects both spin and orbital degrees of freedom simultaneously as a result of the spin-orbit transformation of the wavefunctions, and conventional JT orbital ordering is converted into a magnetic quadrupolar ordering of $J = 3/2$ or $J = 2$ moments. An important consequence of spin-

orbital entanglement is that, distinct from usual orbital order in $3d$ systems, magnetic quadrupolar order breaks not only the point-group symmetry of a crystal but also the rotational symmetry in magnetic space, resulting in anisotropic, non-Heisenberg-type magnetic interactions, such as XY or Ising models. In other words, JT coupling in spin-orbit-entangled systems has a direct and more profound influence on magnetism.

The above discussion is based on the LS -coupling scheme, which is adequate for obtaining the ground state quantum numbers. However, the corresponding wavefunctions, and hence effective g -factors, as well as excited-state energy levels, may get some corrections to LS -coupling results. This is important for the interpretation of the experimental data. Similarly, the admixture of the $t_{2g}^{n-1} e_g^1$ configuration into the ground state t_{2g}^n wavefunctions by SOC and multielectron Coulomb interactions is present for all d^n , and may renormalize the g -factors and wavefunctions.^{5,6} However, these effects cannot split the ground state J -levels, except the $J = 2$ level of the d^2 configuration, as discussed above.

In general, the ground state manifold of transition metal ions in Mott insulators is conveniently described in terms of effective spin (“pseudospin”) \tilde{S} , where $2\tilde{S} + 1$ is the degeneracy of this manifold. For low-spin d^n ions in a cubic symmetry, pseudospin \tilde{S} formally corresponds to effective total angular momentum J (often called J_{eff}), with the exception of the d^2 case with an E_g doublet hosting a pseudospin $\tilde{S} = 1/2$. One has to keep in mind however, that even in the case of cubic symmetry, the pseudospin wavefunctions are different from pure J states because of various corrections (deviations from LS scheme, admixture of e_g states, etc.) discussed above. This is even more so when noncubic crystal fields are present and become comparable to SOC. We will occasionally use both \tilde{S} and J pseudospin notations, depending on convenience (e.g., reserving J for the Heisenberg exchange constant in some cases).

In strong spin-orbit-entangled systems, the notion of pseudospins remains useful even in doped systems, at least at low doping where Mott correlations, and hence the ionic spin-orbit multiplets, are still intact locally. In highly doped systems, a weakly-correlated regime, a conventional band picture emerges, where SOC operates on a single-electron level.

B. Pseudospin interactions in Mott insulators

The key element when considering the interactions among pseudospins is the entanglement of spin and orbital degrees of freedom. In the pseudospin state, various $|L_z, S_z\rangle$ combinations are superposed, forming a composite object. Figure 3 shows two important examples for the d^5 and d^4 cases that will be extensively discussed later. Mixing the spins and orbitals in a coherent way, pseudospins do experience all the interactions that operate both in the spin and orbital sectors, which have

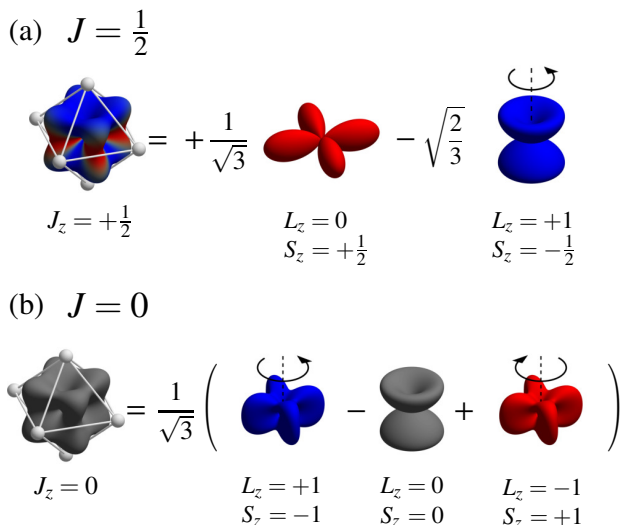


FIG. 3. (a) Decomposition of the $J = 1/2$ Kramer's doublet state of d^5 into $|L_z, S_z\rangle$ components of the single hole in t_{2g}^6 configuration. The effective angular momentum is indicated by the rotating arrow, spin by the color following the convention of Fig. 1. For both contributions, L_z and S_z sum up to $J_z = +1/2$. (b) Similar decomposition of the $J = 0$ two-hole ground state of d^4 . The total orbital angular momentum L_z and spin S_z may be combined in three ways here. The internal compensation in L and S creates a cubic-shaped object showing no spin polarization.

very different symmetry properties. Electron exchange processes conserve total spin, and hence the spin interactions are of isotropic Heisenberg ($\mathbf{S}_i \mathbf{S}_j$) form. The orbital interactions are however far more complex – they are anisotropic both in real and magnetic spaces.^{7–9} In high-symmetry crystals, orbitals are strongly frustrated, because they are spatially anisotropic and hence cannot simultaneously satisfy all the interacting bond directions. Via the spin-orbital entanglement, the bond-directional and frustrating nature of the orbital interactions are transferred to the pseudospin interactions.¹⁰

Moreover, apart from the exchange interactions driven by virtual electron hoppings, there are other contributions to the orbital interactions, especially in the d^1 and d^2 cases. These are mediated by the orbital-lattice JT coupling to the virtual JT-phonons, and by electrostatic multipolar interactions between d -orbitals on different sites.^{11,12} In low-energy effective Hamiltonians, these interactions transform into pseudospin multipolar couplings, driving both structural and “spin-nematic” transitions breaking cubic symmetry in real and pseudospin spaces. The JT-driven interactions are also important in d^4 systems, as they split the excited $J = 1$ levels, and hence promote magnetic condensation.¹³ In the case of d^5 systems with Kramer's-degenerate $J = 1/2$ pseudospins, the effective Hamiltonians are predominantly of exchange origin, as in usual spin-1/2 systems, although JT orbital-lattice coupling still shows up in the fine de-

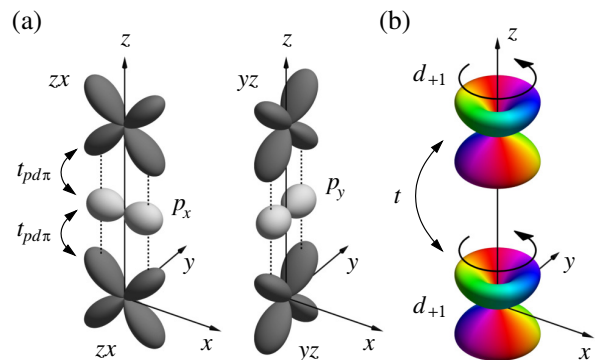


FIG. 4. (a) Hopping via oxygen in the case of 180° M-O-M bonds. The orbital label of the two active t_{2g} orbitals (here zx and yz) is conserved. The third orbital (xy , not shown) cannot connect to the oxygen p states. (b) Combining orbitals into L_α eigenstates with α determined by the bond direction, the above rules lead to a conservation of $L_\alpha = \pm 1$ while the $L_\alpha = 0$ xy -orbital is inactive.

tails of pseudospin dynamics, in the form of pseudospin-lattice coupling.¹³

In general, the low-energy pseudospin Hamiltonians may take various forms depending on the electron configuration d^n and symmetry of the crystal structure. Sensitivity of orbital interactions to bonding geometry is a decisive factor shaping the form of the pseudospin Hamiltonians. We illustrate this by considering spin-orbital exchange processes in two different cases – when metal(M)-oxygen(O) octahedra MO_6 share the corners, and when they share the edges. These two cases are common in transition-metal compounds and are referred to as 180° and 90° bonding geometry, reflecting the approximate angle of the M-O-M bonds. For simplicity, we limit ourselves to the case of d^5 ions with wavefunctions [c.f. Fig. 3(a)]:

$$|f_{\uparrow}\rangle = +\sin\vartheta |0, \uparrow\rangle - \cos\vartheta |+1, \downarrow\rangle, \quad (2.1)$$

$$|f_{\downarrow}\rangle = -\sin\vartheta |0, \downarrow\rangle + \cos\vartheta |-1, \uparrow\rangle, \quad (2.2)$$

where we represent the pseudospin-1/2 Kramer's doublet by f -fermion that is associated with a hole in the full t_{2g}^6 configuration. The spin-orbit mixing angle is determined by $\tan 2\vartheta = 2\sqrt{2}/(1+2\Delta/\lambda)$, where Δ is tetragonal splitting of the t_{2g} orbital level. In the cubic limit of $\Delta = 0$ shown in Fig. 3(a), one has $\sin\vartheta = 1/\sqrt{3}$, $\cos\vartheta = \sqrt{2/3}$.

The individual orbital components of the pseudospins are subject to distinct hopping processes, as dictated by the orbital symmetry combined with the particular bonding geometry (see Figs. 4 and 5). For the corner-sharing 180° case presented in Fig. 4, the nearest-neighbor (NN) hopping Hamiltonian takes the form

$$\begin{aligned} H(180^\circ) &= -t(a_{i\sigma}^\dagger a_{j\sigma} + b_{i\sigma}^\dagger b_{j\sigma} + \text{H.c.}) \\ &= -t(d_{+1i\sigma}^\dagger d_{+1j\sigma} + d_{-1i\sigma}^\dagger d_{-1j\sigma} + \text{H.c.}). \end{aligned} \quad (2.3)$$

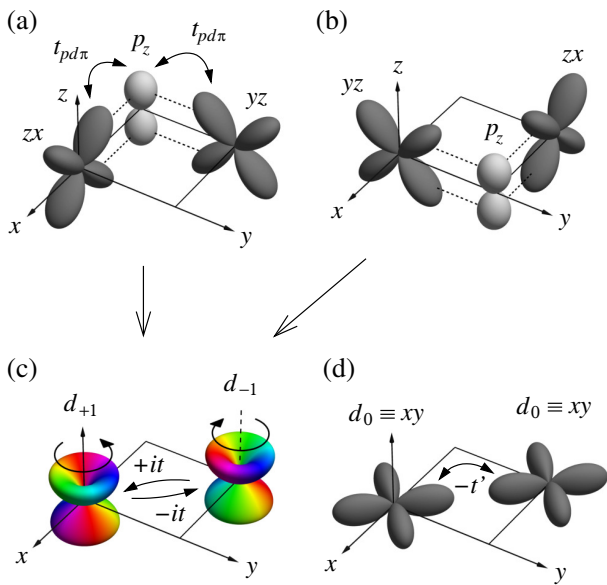


FIG. 5. Hopping in the case of 90° M-O-M bonding geometry. (a), (b) Two t_{2g} orbitals zx and yz are interconnected by the hopping via oxygen p orbitals. They are selected by the orientation of the M_2O_2 plaquette. (c) The complementarity of the orbital labels connected in the M-O-M bridge results in orbital moment non-conserving hopping when considering L_α eigenstates. Here $\alpha = z$ so that $L_z = +1$ is flipped to $L_z = -1$ and vice versa. The corresponding hopping amplitudes are imaginary: $\pm it$. (d) Direct overlap of d orbitals opens an additional hopping channel where the remaining $L_z = 0$ xy -orbital is active.

A summation over the spin index $\sigma = \uparrow, \downarrow$ is assumed. Two of the three t_{2g} orbitals participate in oxygen-mediated hopping with the amplitude $t = t_{pd\pi}^2/\Delta_{pd}$; the active pair $\{a, b\}$ is selected by the bond direction α and may be combined into effective orbital moment $L_\alpha = \pm 1$ eigenstates $|d_{\pm 1}\rangle$. For example, the z bond considered in Fig. 4 picks up $|a\rangle \equiv |yz\rangle$ and $|b\rangle \equiv |zx\rangle$ that form $L_z = \pm 1$ eigenstates $|d_{\pm 1}\rangle = \mp(|yz\rangle \pm i|zx\rangle)/\sqrt{2}$. The third orbital $|c\rangle \equiv |xy\rangle \equiv |d_0\rangle$ cannot couple to the mediating p -orbitals of oxygen for symmetry reasons. Since the NN hopping preserves both spin and orbital in this case, pseudospin is also a conserved quantity. Projecting $H(180^\circ)$ onto the f -doublet subspace defined above, one indeed observes pseudospin-conserving hopping $H = -t_f(f_{i\uparrow}^\dagger f_{j\uparrow} + f_{i\downarrow}^\dagger f_{j\downarrow} + \text{H.c.})$, which should therefore lead to isotropic Heisenberg exchange $H = J(\tilde{S}_i \cdot \tilde{S}_j)$ with $J = 4t_f^2/U$.

The situation in the case of 90° bonding geometry is completely different. As shown in Fig. 5, two bond-selected t_{2g} orbitals $\{a, b\}$ spanning the $|d_{\pm 1}\rangle$ subspace are again active in the oxygen-mediated hopping $t = t_{pd\pi}^2/\Delta_{pd}$, but their labels get interchanged during the hopping: $a \leftrightarrow b$, i.e. $yz \leftrightarrow zx$ for z bond. The third orbital c corresponding to $|d_0\rangle$ participates in direct hopping t' . The two hopping channels are captured by the

NN Hamiltonian:¹⁰

$$\begin{aligned} H(90^\circ) &= t(a_{i\sigma}^\dagger b_{j\sigma} + b_{i\sigma}^\dagger a_{j\sigma}) - t'c_{i\sigma}^\dagger c_{j\sigma} + \text{H.c.} \\ &= it(d_{+1i\sigma}^\dagger d_{-1j\sigma} - d_{-1i\sigma}^\dagger d_{+1j\sigma}) - t'd_{0i\sigma}^\dagger d_{0j\sigma} + \text{H.c.} \end{aligned} \quad (2.4)$$

In contrast to the 180° case discussed above, the t -hopping term does not conserve L_z , but changes it by $\Delta L_z = \pm 2$; $|d_{+1}\rangle \leftrightarrow |d_{-1}\rangle$. Due to spin conservation, the total angular momentum projection has to change by the same amount, i.e. $\Delta J_z = \pm 2$. However, such hopping cannot connect pseudospin-1/2 states (maximal $\Delta J_z = \pm 1$ can be reached by hopping $f_{i\uparrow}^\dagger f_{j\downarrow} + \text{H.c.}$); indeed, projection of the t -term in $H(90^\circ)$ onto pseudospin f -space gives simply zero. This implies that the pseudospin wavefunctions cannot form d - p - d bonding states, and thus the conventional pseudospin exchange term $4t^2/U$ due to hopping t via oxygen ions is completely suppressed.^{10,14} The situation is similar to the e_g orbital exchange in the 90° bonding geometry, where e_g orbitals cannot form d - p - d bonding states and thus no spin-exchange process is possible. As in the e_g case, the pseudospin interactions in the edge-shared geometry are generated by various corrections to the above picture (a direct overlap of pseudospins due to the t' -term, electron hopping to higher spin-orbital levels, corrections to pseudospin wavefunctions due to non-cubic crystal fields, etc.). The resulting pseudospin Hamiltonians are typically strongly anisotropic, and the most important and actually leading term in real compounds is bond-dependent Ising coupling. Figure 6 illustrates how such an interaction emerges due to the t -hopping from ground state $J = 1/2$ to higher spin-orbit $J = 3/2$ levels and subsequent Hund's coupling of the excited electrons in the virtual state. The resulting exchange interaction reads as $H = K\tilde{S}_i^z \tilde{S}_j^z$, and the corresponding coupling constant $K \propto -(J_H/U)4t^2/U$ is of ferromagnetic sign.¹⁴ Considered on honeycomb lattices, this interaction generates the famous Kitaev model where the Ising axis is not global but bond dependent, taking the mutually orthogonal directions x , y , and z on three different NN bonds.¹⁵ This results in strong frustration and a spin-liquid ground state. On the other hand, a direct hopping t' , which conserves both orbital and spin angular momentum, leads to conventional AF Heisenberg coupling $\propto t'^2/U$.

We will later discuss the pseudospin interactions in more detail in the context of some representative compounds, after a brief materials overview.

C. Materials overview

As discussed above, the interactions between spin-orbit-entangled pseudospins critically depend on the bonding geometry, and the ground states are determined by the network of each bonding unit, namely crystal structures. Before discussing the properties of representative materials, it would be instructive to overview

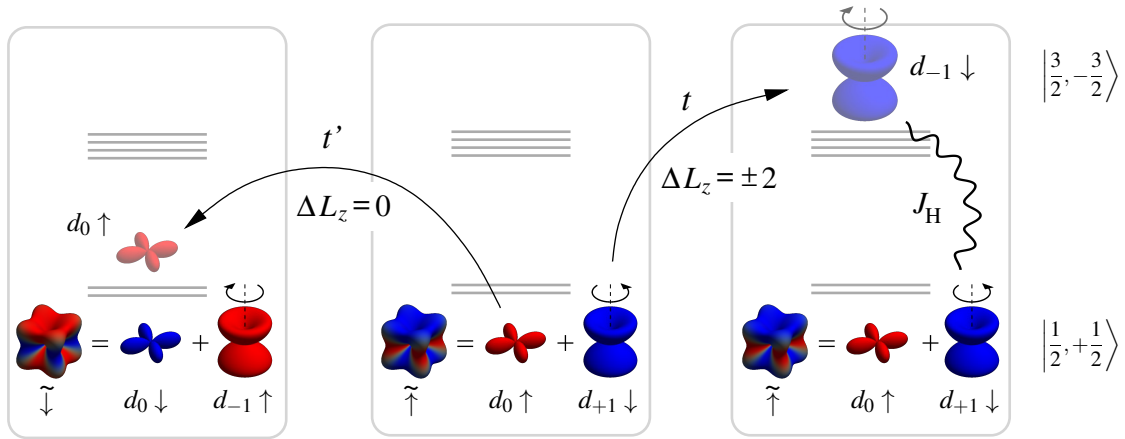


FIG. 6. Virtual processes generating the effective interactions among pseudospins $J = 1/2$ of d^5 configurations in 90° bonding geometry. An M_2O_2 plaquette perpendicular to the z axis as in Fig. 5 is assumed. Compared to Fig. 3(a), here we scale the d_0 , $d_{\pm 1}$ orbitals to visually hint on their relative contributions to the pseudospin wavefunctions. (left part) L_z -conserving direct hopping t' uses the d_0 part of the hole wavefunction and leads to a conventional Heisenberg exchange $\tilde{S}_i \tilde{S}_j$ following the Pauli exclusion principle for the d_0 orbital. (right part) Hopping via oxygen t takes the d_{+1} part of the hole wavefunction and by the L_z flip creates a virtual d^4 configuration combining the original d^5 hole and $J_z = -3/2$ quartet hole. The only option to reach a final state with two $J = 1/2$ pseudospins by the second t hopping is to remove this $J_z = -3/2$ quartet state again, leaving the initial pseudospin directions unchanged during the exchange process. Therefore, the effective interaction is of Ising $\tilde{S}_i^z \tilde{S}_j^z$ type. Hund's exchange J_H between the major $d_{\pm 1}$ parts of the two holes in the virtual d^4 configuration prefers aligned pseudospins on the two sites which results in *ferromagnetic* Kitaev interaction $K \tilde{S}_i^z \tilde{S}_j^z$ with $K < 0$.

the crystal structures that are frequently seen in the $4d$ and $5d$ transition-metal compounds. We will introduce crystal structures comprising the corner-sharing or edge-sharing network of MO_6 octahedra.

1. Corner-sharing network of MO_6 octahedra

The most representative structure with corner-sharing MO_6 octahedra is the perovskite structure with a chemical formula of ABO_3 (A and B are cations). Small transition-metal ions are generally accommodated into the B-site, and the BO_6 octahedra form a three-dimensional corner-sharing network. The stability of the perovskite structure is empirically evaluated by the Goldschmidt tolerance factor $t = (r_A + r_O) / \sqrt{2}(r_B + r_O)$ where r_A , r_B and r_O are the ionic radius of A, B and oxygen ions, respectively. Note that the perovskite structure consists of alternate stacking of AO layer and BO_2 layer. $t = 1$ means that the ionic radii are ideal to form a cubic perovskite structure [Fig. 7(a)] with the perfect matching of the spacings of constituent ions for AO and BO_2 layers. As the ionic radius r_B for $4d$ and $5d$ transition-metal ions is relatively large, the tolerance factor t of $4d$ and $5d$ perovskites are normally less than 1, giving rise to lattice distortions to compensate the mismatch between AO and BO_2 layers. A distorted perovskite structure frequently found in $4d$ and $5d$ transition-metal oxides is the orthorhombic $GdFeO_3$ -type (Space group $Pbnm$) [Fig. 7(b)]. The BO_6 octahedra rotate about the

c -axis and tilt around the $[110]$ direction (Glazer notation: $a^- a^- c^+$ ¹⁶). Because of this distortion, the B-O-B angle is smaller than 180° . Many $4d$ and $5d$ transition-metal perovskites such as $CaRuO_3$, $NaOsO_3$ and $SrIrO_3$ crystallize in the $GdFeO_3$ -type structure.^{17–19}

In addition to the three-dimensional network, the quasi-two-dimensional analogue with 180° bonding geometry is realized in the layered derivatives of perovskite structure. The square lattice of octahedrally-coordinated transition-metal ions is seen in the K_2NiF_4 -type (A_2BO_4) layered structure, where the alternate stacking of $(AO)_2$ - BO_2 layers along the c -axis is formed. Generally, the BO_6 octahedra are tetragonally distorted in the layered perovskites such as Sr_2VO_4 . As in the ABO_3 -type perovskite, the mismatch of ionic radii of A and B cations results in the rotation and the tilting distortion of BO_6 octahedra, making the B-O-B angle less than 180° . For example, the layered iridate Sr_2IrO_4 possesses the rotation of IrO_6 octahedra about the c -axis,²⁰ whereas Ca_2RuO_4 hosts both a rotation and tilting distortion of RuO_6 octahedra.²¹

The $K_2NiF_4(A_2BO_4)$ -type perovskite is an end member of a Ruddlesden-Popper series with a general chemical formula of $A_{n+1}B_nO_{3n+1}$. This formula can be rewritten as $AO(ABO_3)_n [= AO(AO-BO_2)_n]$, which makes it easier to view the crystal structures; there are n -layers of BO_6 octahedra, sandwiched by the double rock-salt-type AO layers as illustrated in Fig. 7(c). Generally, with increasing number of layers, n , the electronic structure becomes more three-dimensional and hence the bandwidth increases, which may induce a metal-insulator transition

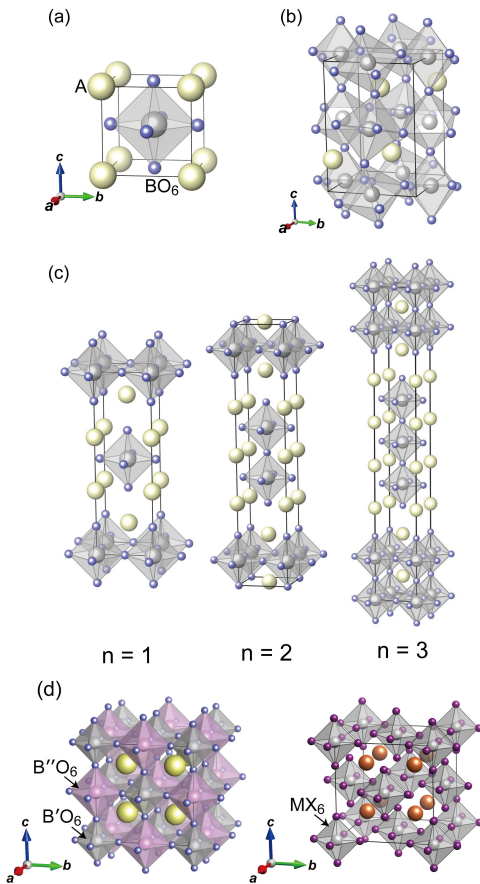


FIG. 7. Crystal structures of perovskite and its derivatives. (a) Cubic perovskite ABO_3 . (b) Orthorhombic perovskite with the $GdFeO_3$ -type distortion. (c) Ruddlesden-Popper series layered perovskite $A_{n+1}B_nO_{3n+1}$. (d) Double-perovskite $A_2B'B''O_6$ (left) and A_2MX_6 -type halides (right). The crystal structures are visualized by using VESTA software.²²

as a function of n .

The double-perovskite structure is a derivative of perovskite, and also called rock-salt-ordered perovskite. In the double-perovskites, two different cations, B' and B'' , occupy the octahedral site alternately and form a rock-salt sublattice. The ordered arrangement of two different B cations is usually seen when the difference of valence state of the two cations is more than 2. Both B' and B'' ions comprise a face-center-cubic (FCC) sublattice. Note that there is neither a direct $B'-O-B'$ bond nor a $B''-O-B''$ bond. The FCC lattice with d^1 or d^2 ions has been proposed to be a possible realization of multipolar ordering of d electrons, and the double-perovskite oxides with magnetic B' and nonmagnetic B'' ions have been studied intensively as will be discussed in Section V. The FCC lattice of d^1 or d^2 ions is also realized in the series of transition-metal halides with a chemical formula A_2MX_6 (A^+ : alkali ion, M^{4+} : transition-metal ion, and X^- : halogen ion),²³ where MX_6^{2-} octahedra and A^+ ions form anti-fluorite-like arrangement. This structure

can be viewed as a B'' -site deficient double-perovskite $A_2M\Box X_6$, where \Box denotes a vacancy. A_2MX_6 crystallizes in a cubic structure with a large A ion such as Cs^+ . M^{4+} ions with an ideal cubic environment form a FCC sublattice, but also form a distorted structure when the size of A ion is small. A wide variety of $4d$ and $5d$ transition-metal elements can be accommodated into this structure.

Another important class of materials with corner-sharing MO_6 octahedra is the pyrochlore oxide with a general formula $A_2B_2O_7$ (more specifically $A_2B_2O_6O'$ where O and O' represent two different oxygen sites) [Fig. 8(a)]. Transition-metal ions are accommodated into the B-cation site, which forms a BO_6 octahedron, whereas the A-cation is surrounded by six O and two O' atoms in a distorted cubic-like environment. The sublattice of the B-cations, as well as that of A-cations, is a network of corner-shared tetrahedra called the pyrochlore lattice [Fig. 8(c)]. The pyrochlore lattice is known to provide geometrical frustration when magnetic moments of constituent ions interact antiferromagnetically. There are many ways to view the pyrochlore structure as described in Ref. [24]. Most conventionally, the B atom is located at the origin of unit cell (Wyckoff position 16c) for the space group $Fd\bar{3}m$ (No. 227, origin choice 2). In this setting, the only tuneable parameters are the lattice constant and the x coordinate of the O site.²⁵ With $x = 0.3125$, the BO_6 forms an ideal octahedron and the B-O-B angle is $\sim 141^\circ$. In $4d$ and $5d$ transition-metal pyrochlore oxides, x is usually larger than 0.3125, and the BO_6 octahedra are compressed along the $[111]$ direction pointing to the center of B-tetrahedra. The compressive distortion gives rise to a trigonal crystal field on B ions and decreases the B-O-B angle between the neighboring octahedra from 141° , which reduces the hopping amplitude and thus bandwidth. When the ionic radius of the A atom becomes smaller, the trigonal distortion is enhanced. A metal-insulator transition is seen as a function of the size of A ions in pyrochlore oxides such as molybdates $A_2Mo_2O_7$ and iridates $A_2Ir_2O_7$ (A: trivalent ions such as rare-earth or Y^{3+}).^{26,27} The trigonal crystal field which splits the t_{2g} manifold potentially competes with SOC.

2. Edge-sharing network of MO_6

As discussed above, the edge-sharing, namely 90° M-O-M, bonding geometry provides magnetic interactions distinct from those in 180° bonds. With the edge-sharing network of MO_6 octahedra, one can realize a variety of lattice structures of interest, such as the triangular lattice in ABO_2 , the honeycomb lattice in A_2BO_3 and the pyrochlore lattice in AB_2O_4 spinels. They can be constructed from the rock-salt structure.

To derive the layered triangular and honeycomb structures from the rock-salt-type $B''^{2+}O^{2-}$ (B'' : transition-metal atom), first consider the rock-salt structure viewed

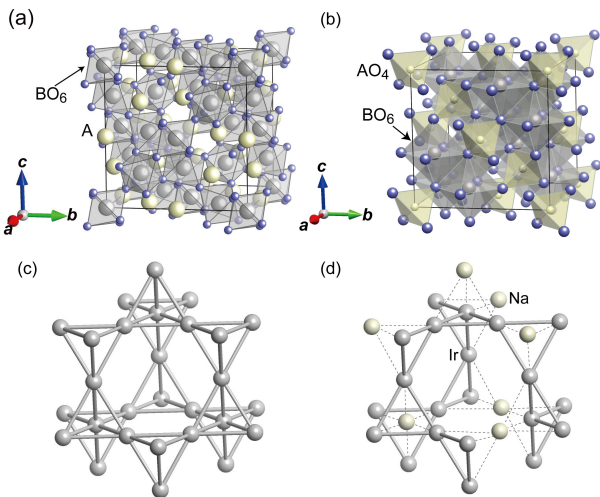


FIG. 8. Crystal structures of (a) pyrochlore oxide $A_2B_2O_7$ and (b) spinel oxide AB_2O_4 . (c) Pyrochlore sublattice comprised by B (or A) atoms of pyrochlore oxide or by B atoms of spinel oxide. (d) Hyperkagome sublattice of Ir atoms found in $Na_4Ir_3O_8$. The pyrochlore sublattice is shared by 3:1 ratio of Ir and Na atoms in an ordered manner.

along the cubic $[111]$ direction [Fig. 9(a)]. It consists of an alternating stack of the triangular B''^{2+} planes and the triangular O^{2-} planes. By replacing every pair of adjacent B''^{2+} planes with an A^+ plane and B'^{3+} plane, we have the layered $AB'O_2$ -type structure with triangular layers of A^+ and B'^{3+} [Fig. 9(b)]. The $B'O_6$ octahedra form the edge-shared triangular lattice. The trivalent B'^{3+} can be replaced by a 2:1 ratio of B^{4+} and A^+ ions. The large difference of valence states between A^+ and B^{4+} cations facilitates the ordered arrangement of two cations in the triangular plane. As a result, the $A_{1/3}B_{2/3}O_2$ layers contain a honeycomb network of BO_6 octahedra connected by three of their six edges [Fig. 9(c)]. The alternate stacking of an A^+ -cation layer and an $A_{1/3}B_{2/3}O_2$ layer corresponds to the chemical formula A_2BO_3 [= $A(A_{1/3}B_{2/3})O_2$] as found in Na_2IrO_3 and Li_2RuO_3 .²⁸ The three-dimensional honeycomb structure of β - Li_2IrO_3 and γ - Li_2IrO_3 can be derived from the rock-salt structure as well, but the ordering pattern of Li^+ and Ir^{4+} ions are different from the $[111]$ ordering described above.^{29,30} Those $4d$ and $5d$ transition-metal oxides with a honeycomb network are attracting attention as a realization of exotic quantum magnetism.

In the ordered rock-salt structures described above, all octahedral voids created by oxygen atoms are filled by cations. The rock-salt structure also has tetrahedral voids that can be occupied by cations. By partially filling the tetrahedral and octahedral voids, a spinel structure AB_2O_4 can be constructed [Fig. 8(b)]. In the spinel structure, B cations form a network of corner-shared tetrahedra as in the pyrochlore oxides. The crucial difference from $A_2B_2O_7$ pyrochlore oxides is that the BO_6

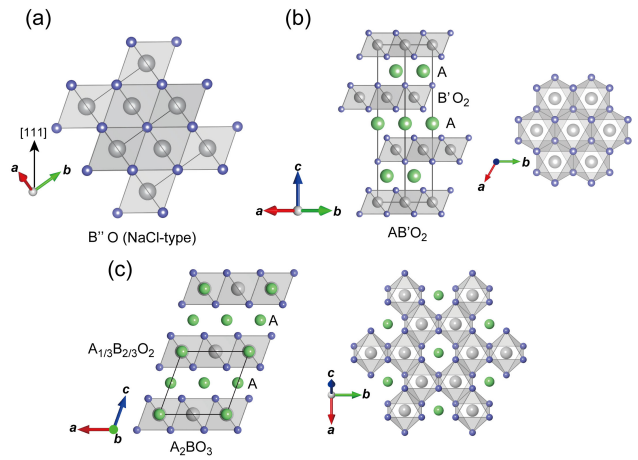


FIG. 9. (a) Rock-salt structure of $B''O$. (b) $AB'O_2$ -type structure formed by replacing B'' with A^+ and B'^{3+} ions which stack alternately along the c -axis. (c) Layered honeycomb structure of A_2BO_3 . The triangular layer of B'^{3+} ions in (b) is substituted by the 2:1 ratio of B^{4+} and A^+ ions forming a honeycomb lattice.

octahedra in the spinel structure are connected by edge-sharing bonds. The number of spinel oxides containing $4d$ or $5d$ transition-metal atoms is rather limited. When multiple cations occupy the pyrochlore B-sublattice, they may form an ordered arrangement. The prominent example is hyperkagome iridate $Na_4Ir_3O_8$.³¹ In $Na_4Ir_3O_8$, the B-site pyrochlore lattice of the spinel is shared in a 3:1 ratio of Ir and Na atoms. The Ir sublattice is viewed as corner-shared triangles in three dimensions, which has been dubbed the hyperkagome lattice [Fig. 8(d)]. The properties of hyperkagome iridate will be discussed in Sections III.C and VI.C.

III. PSEUDOSPIN-1/2 MAGNETISM IN d^5 COMPOUNDS

The collective behavior of d^5 ions with Kramers doublet ground states can be described in terms of a pseudospin-1/2 Hamiltonian. Thanks to the spin one-half algebra, pairwise interactions between pseudospins are reduced to various bi-linear terms. While the forms of these terms are dictated by lattice symmetry, the corresponding coupling constants may vary broadly, depending on the details of the local chemistry of a given material.³² In Sec. II, we emphasized the difference between the 180° and 90° bonding geometry that lead to either conventional Heisenberg interaction or strongly frustrated bond-selective interactions of the Kitaev type. Focusing on these two cases, we now consider a few representative examples of d^5 compounds realizing pseudospin-1/2 physics.

A. 180° M-O-M bonding, perovskites

The perovskite iridate Sr_2IrO_4 has emerged as a model system for understanding the spin-orbit-entangled magnetism of $5d$ electrons. The first experimental evidence for the $J = 1/2$ state was provided by a combination of angle-resolved photoemission spectroscopy (ARPES), optical spectroscopy, and x-ray absorption measurement³³ and later by resonant elastic x-ray scattering,³⁴ which confirmed the complex structure of the d^5 hole.

The relevant pseudospin-1/2 model may be anticipated based on the corner-shared IrO_6 octahedra in the perovskite structure with approximately 180° Ir-O-Ir bonds (the bonds are not completely straight due to 11° in-plane octahedra rotations³⁵). Since the pseudospin wavefunctions overlap well in the d - p - d hopping channel, and hopping is pseudospin conserving as discussed in Sec.II.B, the dominant interaction is represented by Heisenberg coupling. However, there are additional terms which arise due to hoppings to higher level orbitals, tetragonal distortions and octahedral rotations, and these lead to the following NN-interaction Hamiltonian:

$$H = J(\tilde{\mathbf{S}}_i \tilde{\mathbf{S}}_j) + D(\tilde{\mathbf{S}}_i \times \tilde{\mathbf{S}}_j) + A(\tilde{\mathbf{S}}_i \mathbf{r}_{ij})(\tilde{\mathbf{S}}_j \mathbf{r}_{ij}) + J_z \tilde{S}_i^z \tilde{S}_j^z. \quad (3.1)$$

Here, the D term is an antisymmetric Dzyaloshinskii-Moriya (DM) interaction caused by octahedral rotations and A and J_z represent symmetric anisotropy terms. The J_z term is derived from the combined effect of the octahedral rotations and tetragonal fields, while the A term with dipole-dipole-coupling type bond-directional structure is symmetry allowed even in an ideal cubic structure.³⁶ The coupling constants have been calculated in Ref. [14], and vary as a function of tetragonal crystal field, rotation angle etc. This Hamiltonian nicely accounts for a number of properties of Sr_2IrO_4 , including nearly Heisenberg spin dynamics akin to the cuprates.^{37,38}

A closer look in magnon data³⁸ reveals that the model above has to be extended, including longer-range interactions J_2 and J_3 , which turn out to be much larger than in cuprates. This might be related to the fact that $5d$ electrons are more extended spatially, and to the relatively small Mott gap.³³ More recently, it has been shown that the pseudospins in iridates couple to lattice degrees of freedom via a dynamical admixture of higher-lying spin-orbital levels to the ground state wavefunctions,¹³ which explains the observed in-plane magnon gaps,³⁹ and predicts sizable magnetostriction effects breaking tetragonal symmetry below T_N .

In addition to elastic x-ray scattering,³⁴ the spin-orbit-entangled nature of the d^5 ions in Sr_2IrO_4 was detected by resonant inelastic x-ray scattering (RIXS) experiments that observed³⁸ transitions from $J = 1/2$ to $J = 3/2$ levels, directly confirming the level structure shown in Fig. 1. These excitations, dubbed “spin-orbit exciton”, formally behave as a doped hole in a quantum

antiferromagnet moving in a crystal by emitting and absorbing magnons. The resulting exciton-magnon continuum, as well as the expected quasiparticle peak below it, have been indeed observed,⁴⁰ similar to doped holes in antiferromagnetic cuprates. Also like in the hole-doped cuprates, spin-excitation spectra obtained by RIXS on La-doped Sr_2IrO_4 ^{41,42} revealed paramagnons persistent well into the metallic phase.

Encouraged by the above analogies with cuprates, doped Sr_2IrO_4 samples have been studied in the search for unconventional superconductivity. However, experiments on doped Sr_2IrO_4 are severely impeded by difficulties in obtaining clean samples. Techniques beyond conventional chemical doping such as La-substitution producing electron doped $\text{Sr}_{2-x}\text{La}_x\text{IrO}_4$ have to be employed. For example, surface electron doping achieved by potassium deposition on the surface of parent Sr_2IrO_4 enabled ARPES and scanning tunneling microscopy (STM) studies;⁴³⁻⁴⁵ another promising route is ionic liquid gating.^{46,47} Although no clear evidence for superconductivity was so far detected, Fermi surface and pseudogap phenomena as in cuprates have been observed in ARPES^{43,44} and STM experiments.⁴⁵ For more a detailed account on doped Sr_2IrO_4 , we recommend the recent review.⁴⁸

Next, we briefly discuss the bilayer iridate $\text{Sr}_3\text{Ir}_2\text{O}_7$. Being “in-between” quasi-two-dimensional insulator Sr_2IrO_4 and three-dimensional metal SrIrO_3 , this compound is close to the Mott transition, with a small insulating gap.⁴⁹ Nonetheless, pseudospin-1/2 magnons, as well as $J = 3/2$ spin-orbit excitons, have been observed in RIXS experiments^{50,51} showing that the spin-orbit-entangled nature of low-energy states remains largely intact. A remarkable observation is that the magnetic moment direction and magnon spectra in this compound are radically different from those in the sister compound Sr_2IrO_4 . Possible explanations for this have been offered – based on enhanced anisotropic pseudospin couplings⁵¹ and on dimer formation on the links connecting the two layers.⁵²

B. 90° M-O-M bonding, honeycomb lattice

The case of $J = 1/2$ pseudospins on a honeycomb lattice has sparked a broad interest after the proposal of Ref. [14] that the corresponding materials, such as Na_2IrO_3 (see Fig. 9), may realize a Kitaev honeycomb model.¹⁵ Since there is already a vast literature on this topic, including several review articles,⁵³⁻⁵⁸ we will make just a few remarks concerning the “unwanted” (i.e. non-Kitaev) exchange terms that are present in the Kitaev-model candidate materials studied so far.

As explained in Sec.II.B above, the pseudospin-1/2 wavefunctions cannot communicate with each other via the oxygen ions – the corresponding hopping integral is zero in the cubic limit. Finite interactions (albeit not as strong as in 180° case) do originate from higher order pro-

cesses involving spin-orbit $J = 3/2$ virtual states, or from communication of the pseudospins via a direct t' hopping, as illustrated in Fig. 6. Hoppings to higher lying e_g states with subsequent Hund's coupling, as well as pd charge-transfer excitations do also contribute. Phenomenologically, symmetry considerations dictate the following general form of NN interactions^{59–61}

$$H = K\tilde{S}_i^z\tilde{S}_j^z + J(\tilde{\mathbf{S}}_i\tilde{\mathbf{S}}_j) + \Gamma(\tilde{S}_i^x\tilde{S}_j^y + \tilde{S}_i^y\tilde{S}_j^x) + \Gamma'(\tilde{S}_i^x\tilde{S}_j^z + \tilde{S}_i^z\tilde{S}_j^x + \tilde{S}_i^y\tilde{S}_j^z + \tilde{S}_i^z\tilde{S}_j^y), \quad (3.2)$$

which is expressed here for an M_2O_2 plaquette perpendicular to the cubic z axis, as shown in Fig. 5. The first term represents the Kitaev interaction. According to perturbative calculations,^{60–62} the off-diagonal exchange Γ arises from combined t and t' hoppings, while the Γ' term is generated by trigonal crystal fields that modify the pseudospin wavefunctions. Trigonal field also suppresses the bond-dependent nature of the pseudospin interactions,^{10,63} so the cubic limit is desired to support the Kitaev coupling K and to suppress the Γ' term. However, the J and Γ terms, generated by a direct hopping t' and other possible hopping channels, remain finite even in the cubic limit. The crucial parameter here is the M-M distance that controls the magnitude of the direct overlap of the d -wavefunctions.

Apart from NN J , Γ , and Γ' terms, the longer-range (second/third NN $J_{2/3}$) interactions are likely present in many Kitaev materials. These couplings, which are detrimental to the Kitaev spin liquid, are also related to the spatial extension of the $4d$ and $5d$ orbitals, and to the lattice structure “details” such as the presence/absence of cations (e.g. Li or Na) within or near the honeycomb planes [see Fig. 9(c)], opening additional hopping channels.

Nevertheless, the Kitaev-type couplings appear to be dominant in $5d$ -iridates and also $4d$ -ruthenium chloride, as evidenced by a number of experiments (see, e.g., the review [57]), although they are not yet strong enough to overcome the destructive effects of non-Kitaev terms discussed above. So the efforts to design materials with suppressed “unwanted” interactions have to be continued. An interesting perspective in this context may be the employment of $J = 1/2$ Co^{2+} ions, as has been proposed recently.^{64–66} Although the energy scales for the pseudospin interactions are smaller in this case, the less-extended nature of $3d$ wavefunctions may reduce the longer-range couplings, improving thus the conditions for the realization of the Kitaev model.

The non-Heisenberg, bond-dependent nature of the pseudospin interactions is expected to survive in weakly doped compounds, and affect their metallic properties. In particular, it has been suggested that they should lead to an unconventional p -wave pairing.^{10,67–70} However, experimental data on doped d^5 compounds with 90° bonding geometry is scarce, because a “clean” doping of Mott insulators is a challenge in general.

C. Pseudospins-1/2 on frustrated lattices

A combination of geometrical frustration with spin-orbital frustration may open an interesting pathway to exotic magnetism. In fact, the bond-dependent pseudospin interactions have been first discussed in the context of geometrically frustrated triangular¹⁰ and hyperkagome⁷¹ lattices. Here we discuss some spin-orbit-entangled pseudospin-1/2 systems with geometrically frustrated lattices.

1. Hyperkagome iridate $Na_4Ir_3O_8$

Among complex iridium oxides, $Na_4Ir_3O_8$ appears to be the first example of an exotic quantum magnet. In $Na_4Ir_3O_8$, Ir atoms share the B-site pyrochlore lattice of the spinel with Na atoms, and form a network of corner-shared triangles dubbed the hyperkagome lattice, as described in Sec.II.C.2. The hyperkagome lattice is geometrically frustrated if the Ir moments couple antiferromagnetically.

Indeed, $Na_4Ir_3O_8$ displays a strong antiferromagnetic interaction inferred from the large negative Weiss temperature ($|\theta_{CW}| \sim 650$ K) in the magnetic susceptibility $\chi(T)$.³¹ Nevertheless, no sign of magnetic ordering has been seen down to 2 K both in $\chi(T)$ and the specific heat $C(T)$ as shown in Fig. 10. $Na_4Ir_3O_8$ thus appeared as the first candidate for a three-dimensional quantum spin liquid.

In the $\chi(T)$ of $Na_4Ir_3O_8$, a small bifurcation was seen at around 6 K [the inset to Fig. 10(a)]. It was originally interpreted as a glassy behavior due to a small amount of impurity/defects.³¹ However, it has been pointed out from the ²³Na-NMR and μ SR measurements that $Na_4Ir_3O_8$ exhibits a spin-glassy frozen state or quasistatic spin correlation.^{72,73} We note that the presence of such a glassy state may be associated with the disorder of Na ions in the octahedral A-site. Since the successful growth of $Na_4Ir_3O_8$ single crystals was reported recently,⁷⁴ the understanding of its magnetic ground state is advancing.

After the discovery of the spin-liquid behavior in $Na_4Ir_3O_8$, a plethora of theoretical studies have been put forward. In the early days, most of the models have treated the Ir moments as $S = 1/2$ and considered the antiferromagnetic Heisenberg model on the frustrated hyperkagome lattice. The classical model predicted the presence of nematic order.⁷⁵ For the quantum limit, the ground state has been discussed to be either a spin-liquid with spinon Fermi surface or a topological Z_2 spin liquid^{76–78}.

Since the IrO_6 octahedra form an edge-sharing network, as in honeycomb-based iridates, the presence of anisotropic magnetic exchanges such as Kitaev-type coupling is anticipated. The electronic structure calculation showed that SOC of Ir gives rise to a split of the t_{2g} orbitals into spin-orbit-entangled states with $J = 1/2$

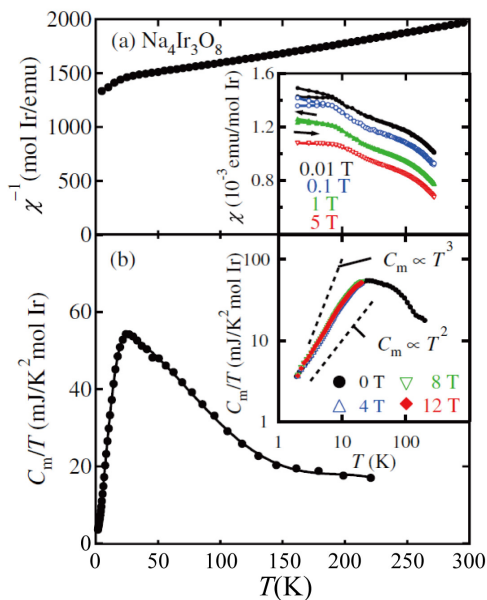


FIG. 10. Temperature dependence of (a) inverse magnetic susceptibility $\chi^{-1}(T)$, and (b) magnetic specific heat C_m divided by temperature. Insets: (a) Temperature dependence of $\chi(T)$ at various magnetic fields. (b) C_m/T at various magnetic fields, showing a power law behavior $C_m(T) \sim T^n$ ($2 < n < 3$) at low temperatures. The figure is reproduced with permission from Ref. [31] (©2007 the American Physical Society).

and 3/2 characters.⁷⁹ In the pure Kitaev limit on a hyperkagome lattice, a nonmagnetic ground state, possibly spin-liquid or valence-bond-solid, has been postulated.⁸⁰ In reality, as in honeycomb iridates, other magnetic exchanges are present, and the antiferromagnetic Heisenberg coupling seems to be the leading term.⁸¹ A microscopic model that takes into account both the Heisenberg term and anisotropic exchanges, such as the DM interaction, predicts the emergence of $q = 0$ noncoplanar order or incommensurate order depending on the magnitude of the anisotropic terms.^{71,82,83} The spin-glass state of $\text{Na}_4\text{Ir}_3\text{O}_8$ may be associated with the presence of such competing magnetic phases.

2. Pseudospin-1/2 on pyrochlore lattice

In addition to the hyperkagome lattice, the pyrochlore lattice of pseudospin-1/2 states with an edge-shared bonding geometry is found in an A-site deficient spinel Ir_2O_4 .⁸⁴ Theoretically, Ir_2O_4 is discussed to host spin-ice-type “2-in-2-out” magnetic correlation and a U(1) quantum spin-liquid state is predicted under tetragonal strain.⁸⁵ Ir_2O_4 has been obtained only in a thin-film form, and its magnetic properties remain yet to be investigated.

The frustrated magnetism of Ir^{4+} moments is also realized in pyrochlore oxides $\text{A}_2\text{Ir}_2\text{O}_7$ (A: trivalent cation).

The electronic ground state of $\text{A}_2\text{Ir}_2\text{O}_7$ depends on the size of the A-ion (ionic radius r_A), which likely controls the bandwidth of Ir 5d electrons.⁸⁶ With the largest r_A in the family of $\text{A}_2\text{Ir}_2\text{O}_7$, $\text{Pr}_2\text{Ir}_2\text{O}_7$ exhibits a metallic behavior down to the lowest temperature measured. With a slightly smaller r_A such as Nd^{3+} , Sm^{3+} or Eu^{3+} , $\text{A}_2\text{Ir}_2\text{O}_7$ shows a metal-to-insulator transition as a function of temperature,⁸⁷ accompanied by a magnetic order. For an even smaller r_A than that of Eu^{3+} , $\text{A}_2\text{Ir}_2\text{O}_7$ remains insulating up to well above room temperature while magnetic ordering takes place only at a low temperature, pointing to the Mott insulating state.²⁷ We focus here on the magnetism of Ir pseudospin-1/2 moments in the Mott insulating ground state. The metallic states of the pyrochlore iridates will be discussed in Sec.VI.B.

For the pyrochlore iridates in the insulating limit, the local electronic state of Ir 5d electrons is primarily of $J = 1/2$ character, but a sizable mixing of the $J = 3/2$ components is present.⁸⁸ The mixing was attributed to the presence of a trigonal crystal field, which is generated not only by the oxygen cage but also by the surrounding cations.⁸⁹ Recently, it turned out that the inter-site hopping plays a dominant role in the $J = 3/2$ mixing. In fact, by suppressing the hopping, a nearly pure $J = 1/2$ state can be realized.⁹⁰

The magnetic interaction between the $J = 1/2$ pseudospins is predominantly attributed to the antiferromagnetic superexchange interaction via oxygen ions, where the Ir-O-Ir angle is approximately 130° . Although the antiferromagnetic Heisenberg model on the pyrochlore lattice is predicted to show no magnetic ordering down to 0 K,⁹¹ a DM interaction is present in the pyrochlore oxides as there is no inversion symmetry between the NN Ir atoms. It was shown in the spin Hamiltonian including Heisenberg and DM interaction on a pyrochlore lattice that the positive DM term gives rise to the all-in-all-out (AIAO) magnetic order, where all the magnetic moments on a tetrahedron of pyrochlore lattice are pointing inward or outward along the local [111] direction [Fig. 11(a)].⁹² On the other hand, when the DM term is negative, noncoplanar XY-type magnetic order appears where the moments lie in the plane perpendicular to the local [111] direction.

The magnetic structure of pyrochlore iridates has been studied by resonant x-ray scattering, and the $q = 0$ magnetic order of Ir moments was revealed in $\text{Eu}_2\text{Ir}_2\text{O}_7$ [Fig. 11(b)]⁹³. The $q = 0$ propagation vector suggests the formation of the AIAO magnetic ordering or the non-coplanar XY antiferromagnetic order, as expected for the presence of DM interactions. In $\text{Sm}_2\text{Ir}_2\text{O}_7$ and $\text{Eu}_2\text{Ir}_2\text{O}_7$, the gapped magnon dispersion revealed by RIXS [Fig. 11(c)] supports the AIAO order of Ir moments.^{94–96} The AIAO magnetic order is discussed to give rise to a Weyl semimetallic state in the vicinity of the metal-insulator transition.⁹⁷

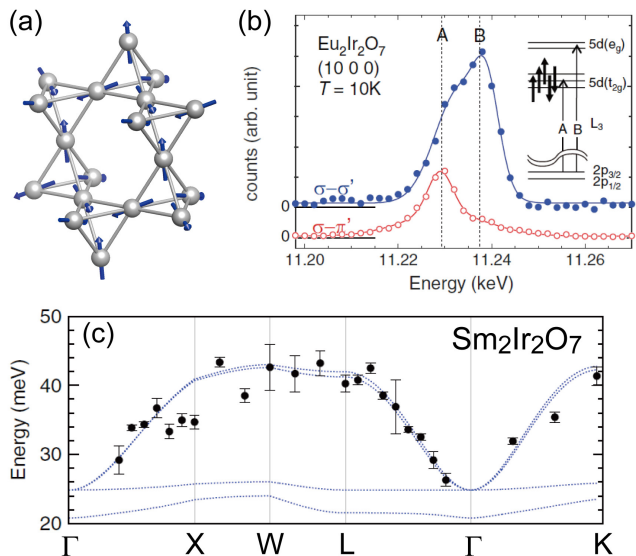


FIG. 11. (a) All-in-all-out (AIAO) magnetic ordering on a pyrochlore lattice. (b) The $q = 0$ magnetic order revealed by resonant x-ray scattering in $\text{Eu}_2\text{Ir}_2\text{O}_7$ at the Ir L_3 absorption edge. The peaks at A(B) correspond to Ir $2p_{3/2} \rightarrow t_{2g}$ ($2p_{3/2} \rightarrow e_g$) excitation, respectively. The strong resonant enhancement at A in the σ - π' channel points to a magnetic scattering. The resonant enhancements in the σ - σ' channel at both A and B originate from anisotropic tensor susceptibility (ATS) scattering. The figure is reproduced with permission from Ref. [93] (©2013 the American Physical Society). (c) The energy dispersion of magnetic excitation of $\text{Sm}_2\text{Ir}_2\text{O}_7$ obtained from RIXS. The black dots are the experimental data points and the blue dotted lines show the calculated magnon dispersion assuming AIAO magnetic order. The figure is reproduced with permission from Ref. [94] (©2016 the American Physical Society).

IV. $J = 0$ SYSTEMS: EXCITONIC MAGNETISM

Perhaps the most radical impact of SOC on magnetism is realized in compounds of $4d$ and $5d$ ions with d^4 configuration, such as Re^{3+} , Ru^{4+} , Os^{4+} , and Ir^{5+} . For these ions with spatially extended d -orbitals, Hund's coupling is smaller than the octahedral crystal field splitting $10Dq$, so all four electrons occupy t_{2g} levels. The resulting t_{2g}^4 configuration has total spin $S = 1$ and threefold orbital degeneracy described by an effective orbital moment $L = 1$. Despite having well defined spin and orbital moments on every lattice site, some d^4 compounds lack any magnetic order. This is because SOC $\lambda \mathbf{S} \cdot \mathbf{L}$ with $\lambda > 0$ binds \mathbf{S} and \mathbf{L} moments into a local singlet state with zero total angular momentum $J = 0$, as shown in Fig. 1.

Nonetheless, these nominally “nonmagnetic” ions may develop a collective magnetism due to interaction effects.^{98,99} Although there are no preexisting local moments in the ionic ground state, the $J = 1$ excitations become dispersive modes in a crystal, and these mobile

spin-orbit excitons may condense into a magnetically ordered state. For this to happen, the exchange interactions should exceed a critical value sufficient to overcome the energy gap λ between $J = 0$ and $J = 1$ ionic states. The condensate wavefunction comprises a coherent superposition of singlet and triplet states and carries a magnetic moment, whose length is determined by the degree of admixture of triplets in the wavefunction. Near the quantum critical point (QCP), the ordered moment can be very small, and the magnetic condensate strongly fluctuates both in phase and amplitude (i.e. rotation of moments and their length oscillations). Formally, this is analogous to magnon condensation phenomenon in quantum dimer systems,¹⁰⁰ but the underlying physics and energy scales involved here are different. While the spin gap in dimer models originates from antiferromagnetic exchange of two spins forming a dimer, the magnetic gap in d^4 systems is of intraionic nature and given by SOC.

Spin-orbit-entangled $J = 0$ compounds are interesting for possible novel phases near the magnetic QCP, which can be driven by doping, pressure, and lattice control. Here, the new element is that $J = 1$ excitons are spin-orbit-entangled objects, and, as we will see shortly, their interactions can be anisotropic and highly frustrating. Thus, $J = 0$ systems with “soft” moments can naturally realize interplay between the two phenomena – frustration and quantum criticality – a topic of current interest.¹⁰¹ As a general property of orbitally degenerate systems, the symmetry and low-energy behavior of spin-orbit excitonic models is dictated by chemical bonding geometry, and we discuss two representative cases below.

A. 180° M-O-M bonding, perovskites

Similarly to the pseudospin-1/2 d^5 case, the straight 180° bond geometry leads to a nearly isotropic model; in the following we thus first focus on the isotropic model of $O(3)$ symmetry. When approaching the excitonic magnet formally, we need to properly reflect the ionic level structure with nonmagnetic $J = 0$ ground state and low-lying $J = 1$ excitations. The most natural way is to introduce hardcore bosons associated with the local excitation $J = 0 \rightarrow 1$. These bosons, called here triplons T , come with the energy cost λ reflected by a local term $\lambda n_T = \lambda T^\dagger T$ and experience various processes corresponding to the exchange interactions between different sites. In the second order in T operators, they include triplon hopping and creation or annihilation of triplon pairs in the symmetry-allowed combination $\propto (T_{+1}T_{-1} - T_0T_0 + T_{-1}T_{+1})_{ij}$, where the indices $(\pm 1, 0)$ give the J_z of the triplons. Instead of J_z eigenstates, it is convenient to use the basis consisting of three triplon operators T_α of Cartesian flavors (“colors”) $\alpha = x, y, z$ defined as

$$T_x = \frac{1}{i\sqrt{2}}(T_1 - T_{-1}), \quad T_y = \frac{1}{\sqrt{2}}(T_1 + T_{-1}), \quad T_z = iT_0, \quad (4.1)$$

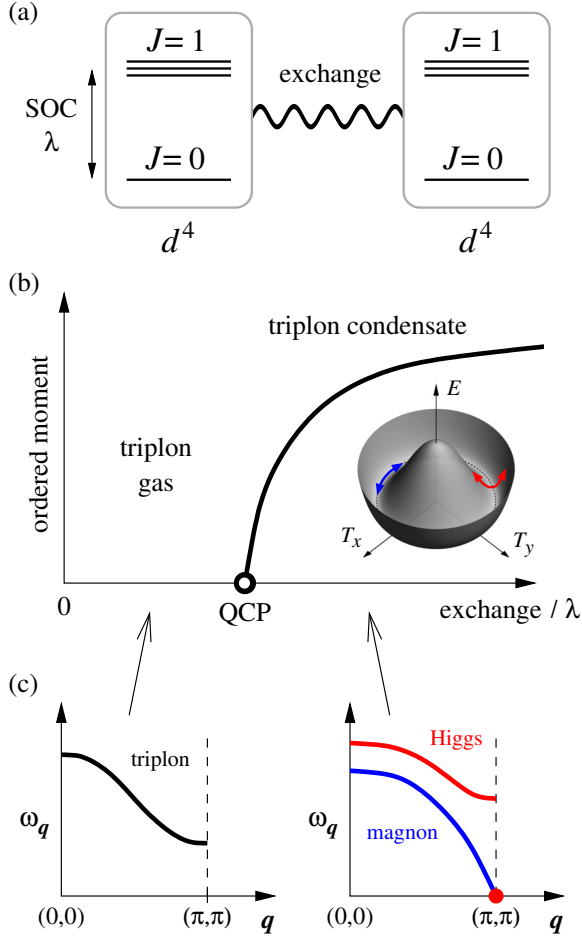


FIG. 12. (a) In the singlet-triplet model for d^4 systems with large SOC, each site is supposed to host nonmagnetic $J = 0$ ground state and low-lying $J = 1$ triplet excitations at the energy λ . Competing with the intrasite SOC gap λ are various intersite exchange processes such as a transfer of a $J = 1$ excitation to a neighboring site or their pairwise creation and annihilation. (b) Ordered moment in an excitonic magnet depending on the ratio of exchange strength versus the local SOC gap λ . The quantum critical point (QCP) separates the large- λ phase where “costly” triplet excitations move in an incoherent way and the phase where the condensate of triplets is established. (c) Schematic dispersions of the elementary excitations. Before the condensation, the elementary excitations are carried by triplets whose dispersion softens near the AF momentum as the QCP is approached. Once the triplon condensate is formed, the oscillations of its amplitude and the moment direction become the new fundamental modes – “Higgs” mode and magnons, respectively. The red spot at (π, π) represents a magnetic Bragg point.

which form a vector \mathbf{T} . The main contribution to the exchange J -Hamiltonian derived in Ref. [98] then takes a manifestly $O(3)$ symmetric form:

$$H = \lambda \sum_i \mathbf{T}_i^\dagger \mathbf{T}_i + \sum_{\langle ij \rangle} J_{ij} \left(\mathbf{T}_i^\dagger \mathbf{T}_j - \mathbf{T}_i^\dagger \mathbf{T}_j^\dagger + \text{H.c.} \right). \quad (4.2)$$

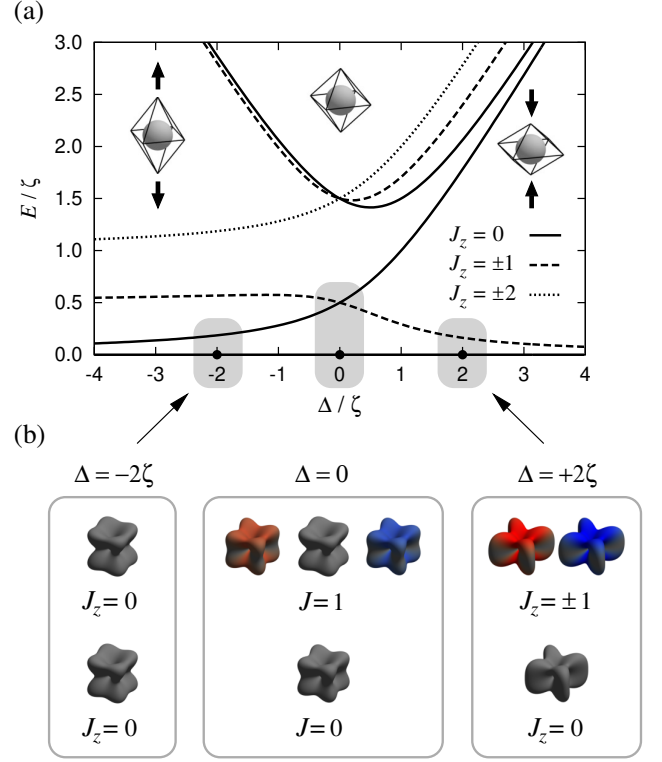


FIG. 13. (a) Splitting of d^4 levels in tetragonal crystal field (measured in units of $\zeta = 2\lambda$). Out of the three triplet excitations, MeO_6 octahedra elongation/compression selects single $J_z = 0$ state or the pair of $J_z = \pm 1$ states. Together with the $J_z = 0$ ionic ground state (evolving from cubic $J = 0$ state), they form a local basis for an effective spin-1/2 (at $\Delta < 0$) or spin-1 (at $\Delta > 0$) low-energy models. (b) Shapes of the relevant low-energy states represented in the same way as in Fig. 1 (electron density is used, not the hole one).

The phase diagram of this model is determined by the competition of the triplon cost λ and superexchange coupling J as schematically shown in Fig. 12(b). At sufficient strength of the superexchange, triplets undergo Bose-Einstein condensation like in spin-dimer systems.¹⁰⁰ However, the physical meaning of triplets is very different here. Since the magnetic moment of a d^4 ion resides primarily on the transition between the $J = 0$ and $J = 1$ states, as described by T , the presence of a triplon condensate with $\langle \mathbf{T} \rangle \propto i e^{i\mathbf{Q}\mathbf{R}}$, where \mathbf{Q} is the ordering vector, directly translates to long-range magnetic order. The resulting magnetic order is characterized also by an unusual excitation spectra, see Fig. 12(c). The condensation is preceded by softening of the three-fold degenerate triplon modes near \mathbf{Q} . After condensation, the modes split, giving rise to a two-fold degenerate magnon branch with XY-type dispersion (i.e. with maximum at $q = 0$) and the amplitude (Higgs) mode of the condensate.⁹⁸ These two hallmarks of soft-spin magnetism can be probed experimentally, as was done in the $J = 0$ model system Ca_2RuO_4 with d^4 Ru^{4+} ions.^{102,103}

The perovskite ruthenate Ca_2RuO_4 was identified as a Mott insulator^{104,105} showing a metal-insulator transition around 360 K¹⁰⁶ and antiferromagnetic order below $T_N \approx 110\text{K}$.^{104,107,108} Early experiments¹⁰⁹ revealed that SOC induces a substantial orbital angular momentum in Ru $4d$ levels, supporting the above $J = 0$ picture. In Ru^{4+} ions, the SOC strength is roughly $\zeta \approx 150$ meV, giving the magnetic gap between $J = 0$ and 1 states of the order of $\lambda = \zeta/2 \approx 75$ meV. Compared to λ , exchange interactions are somewhat smaller in ruthenates and would not be able to overcome such a gap. However, as shown in Fig. 13(a), tetragonal distortion and the associated crystal field Δ splits the $J = 1$ excitation and may reduce the gap significantly. The lower doublet $T_{x/y}$ (for the $\Delta > 0$ case relevant for Ca_2RuO_4) can then condense, giving rise to magnetic order, with the ordered moment in the RuO_2 plane. This scenario points to an interesting possibility of a lattice-controlled QCP (e.g. by strain) instead of by magnetic field or high-pressure as in the dimer system TlCuCl_3 .^{110,111} This also suggests the importance of the Jahn-Teller effect even in $J = 0$ systems, which acts through the splitting of triplon levels and renormalization of the ground state wavefunction.¹³

In Ca_2RuO_4 with $\Delta > 0$, one of the $J = 1$ states is lifted up by the crystal field, and we are left with three low-energy states: ground state singlet and the excited doublet, evolving from cubic $J = 0$ and $J_z = \pm 1$ (or $T_{x/y}$) states, respectively. These three states, whose wavefunctions are shown in the right hand side of Fig. 13(b), can be used as a local basis for an effective spin-1. The resulting $\tilde{S} = 1$ Hamiltonian obtained by mapping Eq. (4.2) onto this basis has the form of the XY model with a large single-ion anisotropy:

$$H = E \sum_i (\tilde{S}_i^z)^2 + J \sum_{\langle ij \rangle} (\tilde{S}_i^x \tilde{S}_j^x + \tilde{S}_i^y \tilde{S}_j^y), \quad (4.3)$$

where E denotes a singlet-doublet excitation gap that is smaller than the singlet-triplet splitting λ in Eq. (4.2) due to a crystal field effect. As a result, the exchange interaction J may overcome the reduced spin gap E and induce magnetic order.

The expected XY -type of magnon dispersion was indeed observed by inelastic neutron scattering on Ca_2RuO_4 .¹⁰² The experimental dispersion presented in Fig. 14(a) additionally features a large magnon gap due to orthorhombicity, which is not included in the above simplified model. The observation of the amplitude Higgs mode is to some extent hindered by its strong decay into a 2D two-magnon continuum (as predicted theoretically^{112,113}), which makes it a very broad feature in the INS spectra near the AF wavevector $\mathbf{Q} = (\pi, \pi)$, see Fig. 14(c). On the other hand, the mode is relatively well defined away from \mathbf{Q} as visible in Figs. 14(a),(b). A more direct probe of the Higgs mode that enters INS spectra at momentum \mathbf{Q} is the Raman scattering in the usually magnetically silent A_g channel. In Ref. [103], a Higgs mode in the scalar channel, “unspoiled” by the two-magnon continuum, was identified in Raman spec-

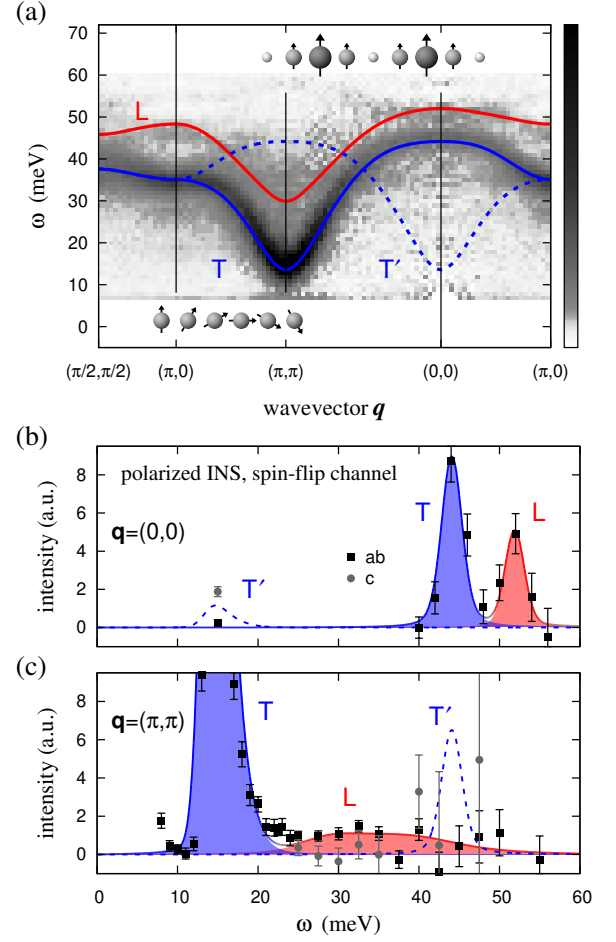


FIG. 14. (a) Magnetic excitations of Ca_2RuO_4 mapped by inelastic neutron scattering. The lines show model dispersions obtained within the model of Ref. [102] (its simpler version is described in the text). The red line indicates longitudinal mode L corresponding to the Higgs mode, and the blue lines represent the in-plane magnon T (solid line) and out-of-plane magnon T’ (dashed line). Upper and lower insets are pictorial representations of the Higgs mode (condensate amplitude oscillations) and magnons (rotations of magnetic moments), respectively. (b) Magnetic response at zero wavevector $\mathbf{q} = (0, 0)$ obtained by polarized INS. In-plane polarization (ab , squares) and out-of-plane polarization (c , circles) were resolved in the experiment. The experimental data are overplotted on top of the theoretical magnetic response that is decomposed according to the polarization of the modes. (c) The same as in (b) for the ordering wavevector $\mathbf{q} = (\pi, \pi)$. All the data are taken from Ref. [102] (©2017 The Authors).

tra of Ca_2RuO_4 , and found to couple to phonons, giving them pronounced Fano-like lineshapes. Such an interaction with lattice modes is natural for triplons, since they have a “shape” inherited from orbitals, and hence couple to lattice vibrations via the Jahn-Teller mechanism as mentioned above.

Spin-orbit exciton condensation and related magnetic

QCP are more likely realized in $4d^4$ compounds such as ruthenates, where SOC and exchange interactions are of comparable scale and their competition can be tuned experimentally. On the other hand, the $5d^4$ ion (Ir^{5+} or Os^{4+}) compounds are typically nonmagnetic, since spin-orbit $J = 1$ excitations are too high in energy, as evidenced by RIXS experiments in $5d$ -electron double perovskites.^{114–116} Weak magnetism detected in the $5d^4$ iridate has been explained as originating from the Ir^{4+} and Ir^{6+} magnetic defects, while the regular Ir^{5+} sites remain indeed nonmagnetic.¹¹⁷

B. 90° M-O-M bonding, honeycomb lattice

When contrasting the 180° and 90° bonding geometries, we encounter a situation analogous to the $J = 1/2$ pseudospin case. While the 180° bonding geometry generates (in leading order) the isotropic $O(3)$ model of Eq. (4.2), discussed above, the bonds with 90° oxygen bridges are highly selective in terms of the active flavors for the triplon interactions. Roughly speaking, when the oxygen-mediated hopping t dominates, each bond allows exchange processes of the type contained in Eq. (4.2) for two triplon flavors only, depending on the bond direction.⁹⁸ For instance, the T_x and T_y bosons are equally active in z -type bonds, while the T_z boson cannot move in that direction. For the honeycomb lattice, the resulting pattern of active triplon pairs is presented in Fig. 15(a). On the other hand, the dominant direct hopping t' leads to the complementary Kitaev-like pattern of Fig. 15(b), with a direct correspondence between the bond direction α and triplon flavor T_α active on that bond.^{118,119} Each of these two cases is strongly frustrated; however, the nature of the corresponding ground states is very different.

In the interaction pattern of Fig. 15(a), each bond shows an $O(2)$ symmetry of the triplon exchange Hamiltonian, that is,

$$H_{ij}^{(z)} = J \sum_{\alpha=x,y} (T_{\alpha i}^\dagger T_{\alpha j} - T_{\alpha i}^\dagger T_{\alpha j}^\dagger + \text{H.c.}) \quad (4.4)$$

for a z -bond $\langle ij \rangle$. However, the global symmetry of the model is only the discrete C_3 one. Namely, there are three zigzag chains (colored differently), along which the individual triplon flavors can move. This arrangement does not support 2D long-range order but instead leads to effective dimensionality reduction like in compass models.¹²⁰ C_3 symmetry is broken by selecting one particular triplon component, with antiferromagnetic correlations along the corresponding 1D zigzag. Zigzag chains interact via the hard-core constraint only (triplon density channel), so there are no phase relations and magnetic order between different chains. The resulting magnetic correlations are highly anisotropic, both in real and spin spaces. This is a combination of an orbital ordered and spin-nematic state, made possible due to spin-orbital entanglement.

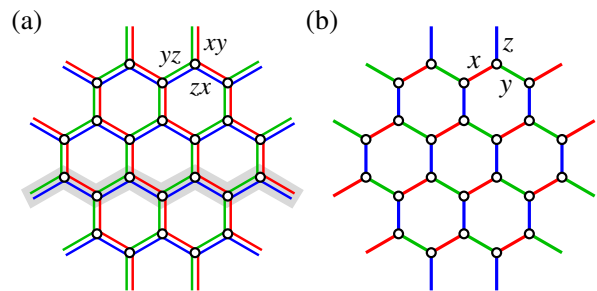


FIG. 15. Patterns indicating active flavors (colors) for bond-selective triplon interactions on honeycomb lattice: (a) Oxygen mediated t -hopping case – XY -type interactions – two flavors are active for a given bond directions (e.g., T_x and T_y on z -type vertical bonds). Each color forms a system of separate zigzag chains (one of the zigzag chains for T_z boson is marked by shading). The symmetry resembles famous compass models where each spin component interacts within its own 1D chain. (b) Direct t' -hopping case – bond dependent Ising-type of interactions. There is one-to-one correspondence between the active triplon color and the bond direction (T_z on z bond, etc), establishing a bosonic analog of the Kitaev model.

The other limit illustrated by Fig. 15(b) may be called a bosonic Kitaev model, following the formal similarity of the triplon exchange Hamiltonian, i.e. $H_{ij}^{(\alpha)} = J(T_{\alpha i}^\dagger T_{\alpha j} - T_{\alpha i}^\dagger T_{\alpha j}^\dagger + \text{H.c.})$ for α -type bonds, to the Kitaev interaction $KS_i^\alpha S_j^\alpha$. As found in Ref. [119], the strong frustration of Kitaev-type prevents a magnetic condensation at any strength of the exchange coupling J relative to spin gap λ . Interestingly, the model shares a number of other features with the spin-1/2 Kitaev model – there is an extensive number of Z_2 conserved quantities, magnetic correlations are strictly short-ranged and confined to nearest-neighbor sites, and the excitation spectrum has a spin gap. However, the strongly correlated triplon “liquid” ground state found in the large exchange limit $J \gg \lambda$ is smoothly connected to dilute triplon gas¹¹⁹ and hence misses the defining characteristics (long-range entanglement and emergent nonlocal excitations) of genuine spin liquids. Consequently, no quasiparticle modes (like Majorana bands in spin-1/2 Kitaev model) are present within the spin gap. Nonetheless, this strongly correlated paramagnet is far from being trivial – in contrast to what is conventional in pure spin systems, magnetic correlations are highly anisotropic and strictly short-ranged even in the limit where the spin gap is very small and the QCP is close by. Magnetic order can be induced by subdominant (non-Kitaev type) triplon interactions, as well as by doping, which suppresses the spin gap. Also, it has been found that triplon excitations acquire nontrivial band topology and protected edge states in a magnetic field.¹¹⁸

By mixing the above two complementary anisotropic limits with the corresponding couplings $J \propto t^2/U$ and

$J \propto t^2/U$ in one-to-one ratio, we recover an isotropic triplon model of Eq. (4.2). Since the honeycomb lattice is not geometrically frustrated, the model shows the same quantum critical behavior as in the square-lattice case, i.e. dispersing triplons condense at a QCP and give rise to long-range antiferromagnetic order. In this context, the ratio of the oxygen-mediated and direct hopping amplitudes t/t' turns out to be an important “handle” determining the degree of frustration (as well as its type) of a singlet-triplet system with 90° bonding geometry.

On the materials side, the Ru-based honeycomb lattice compounds are potential candidates to realize frustrated spin-orbit exciton models. In particular, $\text{Ag}_3\text{LiRu}_2\text{O}_6$,^{121–123} which is derived from Li_2RuO_3 by substituting Ag ions for Li ions between the honeycomb planes, is of interest. While hexagonal symmetry is heavily broken by the structural and spin-orbital dimerization in Li_2RuO_3 ,^{124–126} $\text{Ag}_3\text{LiRu}_2\text{O}_6$ avoids this transition and thus may serve as a model system to study $J = 0$ physics in a nearly ideal honeycomb lattice. This compound shows no magnetic order,^{121–123} which implies that the triplon interactions are either too weak to overcome the spin-orbit gap, or they are dominated by Kitaev-type couplings and thus highly frustrated.

To summarize this section, we note that physics of spin-orbit-entangled $J = 0$ compounds is still in its infancy, and indicate below a few directions for future studies.

(i) Frustrated spin-orbit exciton models, possible exotic phases and magnetic QCP in these models; topological properties of spin-orbit excitations. Experiments in various edge-shared structures and geometrically frustrated lattices, pressure and strain control of magnetic and structural transitions.

(ii) The nature of metallic states induced by electron doping, which injects $J = 1/2$ fermions moving in the background of $J = 0$ states. Fermion hopping is accompanied by creation and annihilation of spin-orbit excitons, which should give rise to a strongly correlated metal. In the case of perovskite lattices with 180° bonding geometry, Ref. [127] suggested that electron doping induces ferromagnetic correlations, and possible triplet pairing mediated by spin-orbit excitations. On the experimental side, several studies^{128–131} found doping driven ferromagnetic state in Ca_2RuO_4 ; interestingly, the recent work has reported also on signatures of superconductivity.¹³² In compounds with 90° bonding geometry, the hopping rules are different and interactions are frustrated; studies of doping effects in such systems may bring some surprises.

V. MULTIPOLAR PHYSICS IN d -ELECTRON SYSTEMS WITH STRONG SPIN-ORBIT COUPLING

Multipolar ordering in Mott insulators covers a whole host of phenomena, ranging from the relatively standard

quadrupole ordering of e_g electrons due to a cooperative Jahn-Teller effect^{7,10} to the formation of bond multipoles in highly quantum-entangled frustrated magnets.^{133,134}

In the absence of significant SOC, the orbital and spin degrees of freedom typically order at different temperatures. At high temperature the cooperative Jahn-Teller effect drives both a structural distortion of the lattice and an associated orbital quadrupole order, while at lower temperature the exchange interaction causes the spins to order. Strong SOC ties together the spin and orbital degrees of freedom, negating the simple picture of separate transitions. As a consequence, the intermediate phase picks up a spin contribution to the quadrupole order, and at the same time the two transitions tend to get pushed closer together in temperature.

The introduction of strong SOC also opens up the possibility of unusual types of interactions, in particular higher-order biquadratic and triatic terms in the Hamiltonian. These interactions can drive more unusual types of multipolar order, such as an octupolar ground state similar to those found in f -electron systems,^{135,136} or, when combined with frustration, cause the multipolar order to melt away, leaving behind a multipolar spin-liquid.

A. Quadrupole ordering

The idea of tensor order parameters, familiar from the theory of classical multipole ordering, can be readily generalised to the quantum case. Just as dipolar order is associated with a non-zero expectation value of the vector $\langle \mathbf{J} \rangle$, quadrupole order is associated with a finite expectation value of the rank-2 tensor,

$$Q_i^{\mu\nu} = \frac{1}{2} \langle J_i^\mu J_j^\nu + J_i^\nu J_j^\mu \rangle - \frac{\langle \mathbf{J}_i \cdot \mathbf{J}_j \rangle}{3} \delta^{\mu\nu}, \quad \mu, \nu \in \{x, y, z\} \quad (5.1)$$

where the site indices i, j can refer to the same or different sites.

1. Quadrupoles in d^1 systems

Quadrupole ordering is very common in strongly spin-orbit-entangled d^1 systems, since d^1 ions with a $J = 3/2$ ground state are Jahn-Teller active, as discussed in Section II.A. The onset of quadrupole order occurs when the degeneracy of the $J = 3/2$ quadruplet is split, selecting a low energy $J_z = \pm 1/2$ or $J_z = \pm 3/2$ doublet. These doublets have a quadrupolar charge distribution (see Fig. 1), as opposed to the cubic charge distribution of the $J = 3/2$ quadruplet, and thus quadrupolar ordering occurs simultaneously with a structural transition in which the local symmetry of the d^1 ions is reduced.

The driving force for the quadrupole-ordering transition comes predominantly from electrostatic and Jahn-Teller interactions, with a helping hand from the exchange interaction. A good way to see this theoretically

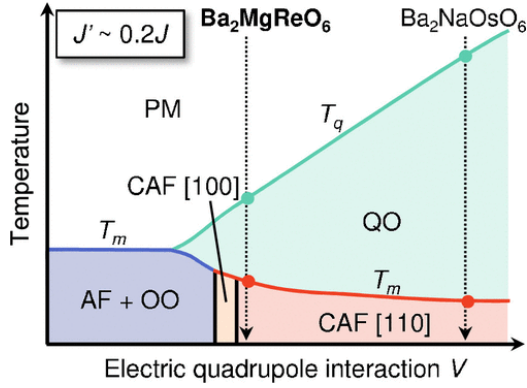


FIG. 16. Schematic phase diagram proposed for strongly spin-orbit coupled d^1 ions. For a large enough interaction V there are two phase transitions as a function of temperature, with a high-temperature transition into a quadrupole ordered (QO) phase followed by a low-temperature transition into one of various dipolar phases, including antiferromagnetic (AF) and canted antiferromagnetic (CAF[100], CAF[110]) orders. The figure is reproduced with permission from Ref. [137] (©2019 The Physical Society of Japan).

is to project the well-known interactions for the 6-fold degenerate t_{2g} manifold of electron configurations into the $J = 3/2$ quadruplet.¹³⁸ In addition to the usual bilinear interactions, the resulting effective Hamiltonian also contains large biquadratic interactions, such as $(J_i^z)^2(J_j^z)^2$, between neighbouring sites. It has been known for a long time that these can be rewritten as quadrupole-quadrupole interactions,^{139–141} and so it is not surprising that they favour quadrupole ordering.

Double-perovskite oxides [Fig. 7(d)] provide some of the cleanest material realisations of spin-orbit-entangled d^1 Mott insulators. The wide spacing of the magnetic ions makes them good Mott insulators with small inter-site interactions, and allows a cubic ionic environment to be retained to low temperature. Figure 16 illustrates a generic phase diagram proposed for d^1 systems with double-perovskite structure.¹³⁷

While none of the known double-perovskite materials have a completely vanishing dipolar magnetic moment, as would be expected for isolated $J = 3/2$ ions (see Sec.II.A), the magnetic moments are small, indicating only weak hybridisation with the surrounding oxygen ions. For example $\text{Ba}_2\text{NaOsO}_6$ has an effective moment of approximately $0.6 \mu_B$.¹⁴³ It also shows two transitions, with a higher temperature structural transition at $T_q = 9.5$ K suggestive of the onset of quadrupolar order, and a lower temperature transition at $T_m \approx 7.5$ K into a magnetically ordered phase.^{143–145} However, since the symmetry above T_q is likely tetragonal rather than cubic, as suggested by the approximately $R\ln 2$ entropy recovery above T_q ,¹⁴³ it is not clear how effectively the system explores the full $J = 3/2$ manifold at higher temperatures.

A similar story is found in $\text{Ba}_2\text{MgReO}_6$, where there is

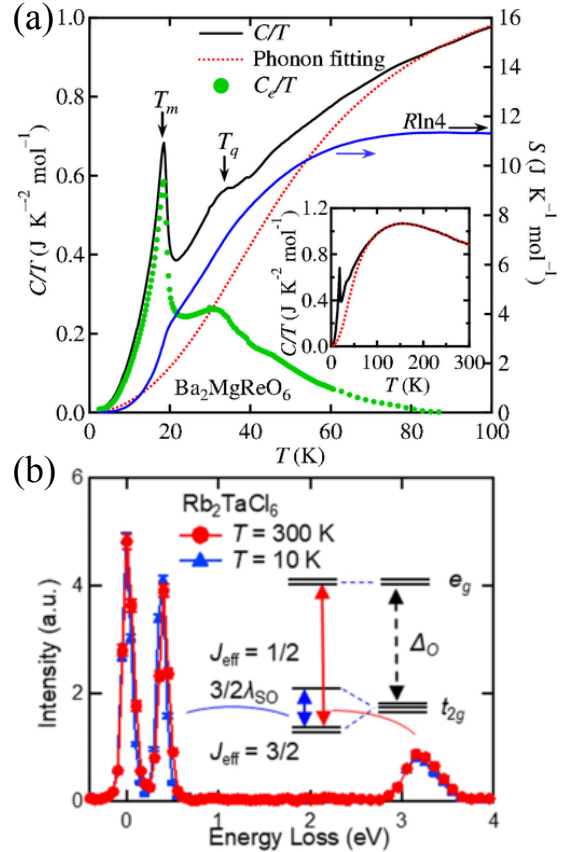


FIG. 17. Evidence for the formation of a strongly spin-orbit-entangled $J = 3/2$ state. (a) Recovery of $R\ln 4$ entropy in $\text{Ba}_2\text{MgReO}_6$ at high temperatures, taken with permission from Ref. [137] (©2019 The Physical Society of Japan). (b) Ta L_{3} -edge RIXS spectrum showing the splitting of the t_{2g} level by SOC. Reproduced with permission from Ref. [142] (©2019 the American Physical Society).

an effective moment of about $0.7 \mu_B$, a high-temperature transition at $T_q \approx 33$ K and a low-temperature transition at $T_m \approx 18$ K to a similar magnetically ordered state to $\text{Ba}_2\text{NaOsO}_6$.^{137,146} However, unlike $\text{Ba}_2\text{NaOsO}_6$ the high temperature structure is cubic, and heat capacity measurements reveal that the full $R\ln 4$ entropy of the $J = 3/2$ multiplet is obtained above about 80 K, as shown in Fig. 17(a).¹³⁷ A small distortion of ReO_6 octahedra was observed below T_q , which is consistent with quadrupole ordering.¹⁴⁷

The closely related A_2TaCl_6 ($\text{A} = \text{Cs}, \text{Rb}$) family appears to provide a particularly good realisation of the $J = 3/2$ state, as can be seen from the small effective magnetic moment of $0.2 - 0.3 \mu_B$.¹⁴² The suitability of the $J = 3/2$ description has been confirmed by RIXS experiments [Fig. 17(b)] and the recovery of the expected $R\ln 4$ entropy at high temperature. As with the double perovskite oxides, two transitions are observed, with the upper transition at $T_q \approx 30$ K for Cs and $T_q \approx 45$ K for Rb and the lower transition at $T_m \approx 5$ K for Cs and $T_m \approx 10$ K for Rb. The upper transition is associated

with a structural transition from cubic to compressed tetragonal, and is suggestive of a ferro-quadrupolar phase forming via selection of the $J_z = \pm 1/2$ doublet.

2. Quadrupoles in d^2 systems

Quadrupolar order for d^2 ions can be expected either from ordering of the low-lying nonmagnetic E_g doublet (see Fig. 2), or driven by a combination of electrostatic, Jahn-Teller and exchange interactions acting within the full $J = 2$ quintuplet.¹⁴⁸ However, there is currently a lack of materials showing the type of double quadrupolar and magnetic transitions observed in many d^1 compounds.

B. Octupole ordering

Octupole phases involve the ordering of the rank-3 tensor,

$$O_i^{\mu\nu\xi} = \overline{\langle J_i^\mu J_j^\nu J_k^\xi \rangle}, \quad \mu, \nu, \xi \in \{x, y, z\}, \quad (5.2)$$

in the absence of dipolar or quadrupolar order, where the bar indicates symmetrisation over the superscripts.

1. Octupoles in d^1 systems

A candidate to realise octupolar order in the absence of any concomitant dipolar order is the material Sr_2VO_4 with perovskite structure. Although V^{4+} ($3d^1$) is not usually thought of as a strongly spin-orbit coupled ion, the combination of SOC and a tetragonal elongation of the oxygen octahedra conspire to select a $J_z = \pm 3/2$ lowest-energy doublet from the t_{2g} manifold, as can be seen in Fig. 18(a).¹⁴⁹ Projection of the usual exchange Hamiltonian for t_{2g} electrons into this ground state doublet reveals a checkerboard ground state of alternating $|\psi\rangle = (|3/2\rangle \pm |-3/2\rangle)/\sqrt{2}$ states, which corresponds to a staggered octupolar order. One possible signature of this octupolar order would be a Goldstone mode with vanishing magnetic response at low energies, potentially visible in inelastic neutron scattering, as shown in Fig. 18(b). Experimental studies are consistent with the local level scheme proposed for the V ions, but the question of whether the ground state is octupolar ordered remains open.^{150–153}

2. Octupoles in d^2 systems

Octupolar order has been suggested to be realised in the d^2 double perovskite family Ba_2MOsO_6 ($M = \text{Zn}, \text{Mg}, \text{Ca}$).^{154,155} While phase transitions are observed at approximately 30 K (Zn) and 50 K (Ca, Mg), there is no associated development of dipolar magnetic order.^{155–157}

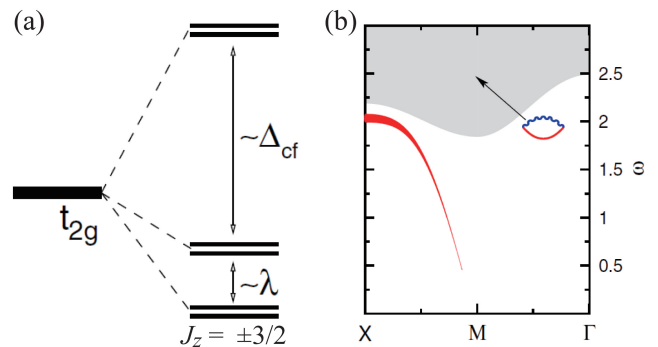


FIG. 18. Local states and collective excitations in Sr_2VO_4 . (a) Splitting of the V^{4+} t_{2g} levels by a tetragonal crystal field Δ_{cf} and spin-orbit coupling λ results in a $J_z = \pm 3/2$ lowest-energy doublet hosting octupolar moment. (b) Prediction for the magnetic response associated with octupolar order. There is a sharp dispersive band of octupolar-wave excitations below the continuum, whose spectral weight in magnetic channel (shown by line width) disappears approaching the octupolar Bragg point at $M = (\pi, \pi)$, reflecting the absence of dipolar order in the ground state. The energy ω is in units of $J = t^2/U$. The figures are taken with permission from Ref. [149] (©2009 the American Physical Society).

Furthermore, the development of quadrupolar order is incompatible with the absence of detectable lattice distortion. At the same time the recovery of only $R \ln 2$ of entropy at temperatures considerably above the transition is indicative of a low-lying doublet, and matches the expected E_g - T_{2g} splitting shown in Fig. 2.

From a theoretical point of view, projection of the interactions between t_{2g} electrons into the $J = 2$ quintuplet shows the importance of bitriatic interactions, such as $(J_i^z)^3 (J_j^z)^3$.^{148,154} These can be rewritten as interactions between octupoles, and, if large enough compared to competing bilinear and biquadratic interactions, can drive the formation of octupolar order. This may provide a mechanism for selecting octupolar order with a ferro-octupolar ground-state wavefunction that is a complex mix of the E_g states as shown in Fig. 2(c), and in terms of J^z states is given by $|\psi\rangle = \frac{1}{2}|2\rangle + \frac{i}{\sqrt{2}}|0\rangle + \frac{1}{2}|-2\rangle$.^{154,155} The breaking of time-reversal symmetry at the transition supports this scenario.^{156,157}

C. Multipoles and frustration

Often more interesting than those systems that show robust multipolar order, are those that combine multipolar order with spin-liquid behaviour, or those that avoid multipole ordering and instead form spin liquids with multipolar correlations. This type of behaviour is associated with frustration, which arises in myriad ways in strongly spin-orbit-entangled systems due to the interplay of lattice geometry with directional-dependent exchange and higher-order biquadratic and bitriatic inter-

actions.

1. d^1 on the FCC lattice

While not a spin liquid, the double perovskite Ba_2YMoO_6 does form a valence-bond glass, in which a disordered pattern of spin-singlet dimers freezes at temperatures below about 50 K, as can be seen in Fig. 19.^{158–161}

One suggestion is that this could be associated with a hidden $SU(2)$ symmetry that can emerge from the complicated and apparently unsymmetric Hamiltonian between $J = 3/2$ states.^{138,162} Solving this Hamiltonian for 2 sites, i and j , gives a lowest-energy singlet state $|\psi\rangle = (|1/2\rangle_i|-1/2\rangle_j - |-1/2\rangle_i|1/2\rangle_j)/\sqrt{2}$, and, extending this to the FCC lattice, results in a degenerate set of singlet dimer coverings with lower energy than any magnetically ordered state.¹⁶² The idea is that in the material a small disorder is responsible for selecting one of the many degenerate dimer configurations, resulting in a dimer glass. This idea is appealing, and, due to the nature of the excitations above the dimer states, gives an explanation for the experimentally determined soft gap, but there remains the question of whether Jahn-Teller interactions, active in d^1 systems, play an important role.

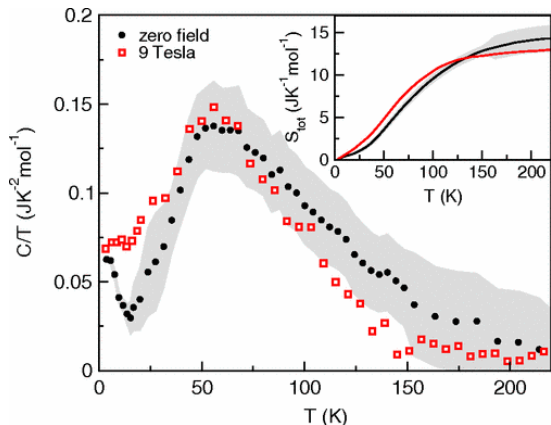


FIG. 19. Valence-bond glass formation in Ba_2YMoO_6 . Heat capacity measurements show no evidence of a phase transition, but do show evidence for a gradual freezing, centred on a broad maximum at about 50 K. This suggests the formation of an amorphous valence-bond state, with a distribution of triplet excitation energies. The figure is reproduced with permission from Ref. [158] (©2010 the American Physical Society).

2. d^2 on the pyrochlore lattice

The material $\text{Y}_2\text{Mo}_2\text{O}_7$ provides an example of how spin-glass and potentially spin-liquid physics can emerge out of a quadrupolar phase.¹⁶³

The Mo^{4+} ions form a pyrochlore sublattice and sit in oxygen octahedra that have a large trigonal distortion at all temperatures, with band structure calculations suggesting that the characteristic energy scale of the trigonal splitting is more than 100 meV¹⁶⁴ [see Fig. 20(a)]. When combined with SOC this results in a low energy $J_z = \pm 2$ doublet with quadrupolar symmetry, well separated from higher energy states, and with the z axis orientated along the local in/out axes of the Mo tetrahedra, as shown in Fig. 20(b).¹⁶⁵ Since there are no interactions that can transform $J_z = \pm 2$ states into one another, the Hamiltonian must be dominated by Ising interactions between the effective spins.^{164–166} This would suggest that either an all-in-all-out ordered state or a spin-ice-like disordered 2-in-2-out configuration should be realised. However, neutron scattering experiments suggest that spin degrees of freedom alone are insufficient to describe the low-temperature behaviour of the system.¹⁶⁷

Evidence for what else needs to be taken into account comes from x-ray and neutron pair distribution analyses, which show that the Mo ions are not forming a perfect pyrochlore lattice, but instead their positions are shifted towards or away from the tetrahedral centres in a disordered 2-in-2-out pattern [see Fig. 20(c)].¹⁶⁸ The experiments further show that the oxygen octahedra are dragged along by the Mo ions, resulting in very little change in the local crystal-field environment, but large variations in the Mo-O-Mo bond angles, with individual bond angles dependent on the details of the 2-in-2-out lattice displacements. Deviations from the average Mo-O-Mo bond angle are expected to result in large changes to both the strength and sign of the exchange interactions [see Fig. 20(d)], resulting in a large coupling between the lattice and spin degrees of freedom and a resulting distribution in the exchange interactions.^{164,165} As such, these materials are nice examples of the interplay of SOC with strong magneto-elastic coupling.

At low temperatures $\text{Y}_2\text{Mo}_2\text{O}_7$ shows spin-glass behaviour,^{163,169} and a number of explanations have been put forward to explain this.^{164–167,170} One possibility is that the low-temperature spin-glass state freezes out of an intermediate-temperature spin-lattice-liquid state, in which the strong magneto-elastic coupling ties together the spin and lattice degrees of freedom, but the system remains dynamic and explores an extensive set of low-energy configurations.¹⁶⁵

VI. SPIN-ORBIT-COUPLED EXOTIC METALS AND NON-TRIVIAL TOPOLOGICAL PHASES

In the previous sections, we discussed the spin-orbit-entangled electronic phases in Mott insulators. However, the Mott insulating state of $4d$ and $5d$ transition-metal oxides is not so robust and often close to a metal-insulator transition. In fact, metallic ground states are also frequently observed. In the itinerant limit, the spin-orbit-entangled states form bands which may be understood

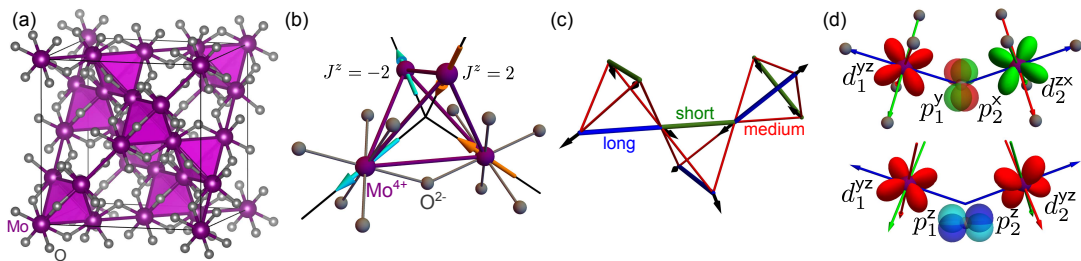


FIG. 20. The interplay of spin and lattice degrees of freedom in $Y_2Mo_2O_7$. (a) Average positions of Mo and O ions, showing the pyrochlore lattice of Mo ions. (b) $J_z = \pm 2$ states represented as Ising spins pointing along the in/out (local z) axes of the Mo tetrahedra. (c) Mo ions displace into or away from tetrahedral centres, creating long, short and medium length Mo-Mo separations. (d) Superexchange paths in the neighbouring MoO_6 octahedra: (upper part) “ π -type” superexchange path that dominates when the Mo’s form an undistorted pyrochlore lattice; (lower part) additional “ σ -type” superexchange path that becomes increasingly important the more the Mo-O-Mo bond angle is changed from its average value. The figures are reproduced with permission from Ref. [165] (©2019 the American Physical Society).

in the framework of jj -coupling. The strong SOC of $4d$ and $5d$ electrons can drastically modify the band structure and may give rise to exotic metallic states, potentially with nontrivial topological character. The emergence of exotic phases such as nodal-line semimetals, Weyl semimetals, and topological Mott insulators has been theoretically discussed. Compared to typical topological semimetals composed of s and p electrons, the presence of electron correlations in these oxides with d -electrons is expected to provide a distinct physics of correlated topological materials. We review in this section the exotic metallic states in perovskite and pyrochlore iridates, as well as in the doped hyperkagome. In addition to iridates, the recently verified hidden multipolar phase and possible unconventional superconductivity in the pyrochlore rhenate will be discussed.

A. Orthorhombic perovskite $AIrO_3$ ($A = Ca, Sr$) with Dirac line node

As discussed in Sec.III.A, the layered perovskites Sr_2IrO_4 and $Sr_3Ir_2O_7$ are Mott insulators with localized $J = 1/2$ pseudospins. In this series of Ruddlesden-Popper perovskite $Sr_{n+1}Ir_nO_{3n+1}$ ($n = 1, 2, \dots$), the Ir $5d$ bandwidth is expected to increase as a function of the number of IrO_2 planes, n . $SrIrO_3$, which corresponds to the limit of $n = \infty$, crystallizes in an orthorhombic perovskite with rotation and tilting distortion of IrO_6 octahedra (space group $Pbnm$), illustrated in Fig. 7(b).¹⁹ This orthorhombic perovskite is a metastable phase stabilized under high-pressure or in a thin-film form; at ambient pressure, $SrIrO_3$ crystallizes in a distorted 6H-type perovskite structure.¹⁹

The orthorhombic perovskite $SrIrO_3$ was shown to be metallic from the transport and optical properties.^{49,171} It is in fact a semimetal with a small carrier density, which is produced by an interplay of crystalline symmetry and strong SOC. If there were no rotations and tilts

of IrO_6 octahedra, cubic $SrIrO_3$ would have a half-filled $J = 1/2$ band with a moderate bandwidth. When the rotations and the tiltings of IrO_6 are incorporated, the bands are back-folded, and many crossing points in the $J = 1/2$ bands show up. The incorporation of SOC opens a gap at many of the crossing points, which makes the system close to a band insulator with 20 d -electrons per unit cell with four Ir atoms. In reality, the presence of symmetry-protected band crossing and the overlap of split bands give rise to a semimetallic state.¹⁷²

The semimetallic band structure of $SrIrO_3$ hosts the Dirac bands near the Fermi energy E_F , which prevents a gap opening. A density functional theory calculation and a tight-binding analysis showed the two interpenetrating Dirac dispersions around the U-point of the Brillouin zone, which yield a nodal-line [Fig. 21(b)].^{173,174} The Dirac nodes are protected by the nonsymmorphic symmetry of the space group $Pbnm$, which contains two glide symmetries, in addition to space- and time-reversal symmetries.^{175,176} The Dirac points are located slightly below E_F , and there are other heavy hole bands crossing E_F to retain the charge neutrality. The presence of linearly dispersive electron bands was confirmed by an ARPES measurement of thin-films.¹⁷² We note that the ambient pressure phase of $SrIrO_3$, crystallizing in a monoclinic $C2/c$ structure, is also a Dirac semimetal protected by the nonsymmorphic symmetry (c -glide).¹⁷⁷

One of the characteristic features of Dirac semimetals is the presence of highly mobile carriers, which have been indeed identified in the perovskite $CaIrO_3$, isostructural to $SrIrO_3$. A carrier mobility as large as $60,000 \text{ cm}^2/\text{V}\cdot\text{s}$ is observed at low temperatures, as shown in Fig. 22.¹⁷⁸ The remarkably high mobility is discussed to be attributed to the proximity of Dirac nodes to E_F .¹⁷⁸ Because of the smaller ionic radius of Ca^{2+} as compared to that of Sr^{2+} , $CaIrO_3$ inherits larger rotation and tilting of IrO_6 octahedra, which reduces the bandwidth and enhances electron correlations. The strong correlation renormalizes the band structure and places the Dirac

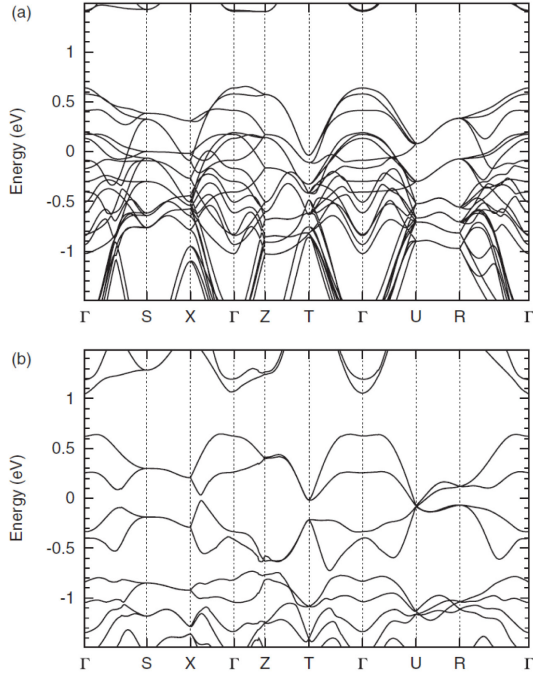


FIG. 21. Band structures of SrIrO₃ obtained from LDA + U calculation with Hubbard $U = 2$ eV: (a) without SOC, and (b) with SOC $\zeta = 2\zeta_{at}$ (ζ_{at} is atomic spin-orbit coupling). The figure is reproduced with permission from Ref. [173] (©2012 the American Physical Society).

nodes near E_F .

It is important to unravel the key factor determining the evolution from a 3D Dirac semimetal to a magnetic insulator in the series of Sr_{n+1}Ir_nO_{3n+1}. In bulk form, Sr_{n+1}Ir_nO_{3n+1} with $n \geq 3$ is not stable at ambient pressure and difficult to grow. As an alternative approach to track the metal-insulator transition, a (001) superlattice comprising SrIrO₃ and nonmagnetic SrTiO₃ layers, i.e. [(SrIrO₃)_m/SrTiO₃], has been designed.¹⁷⁹ By increasing the number of SrIrO₃ layers m , the dimensionality, and thus the bandwidth, of SrIrO₃ layers can be controlled. The metal-insulator transition takes place at around $m = 3$ as shown in Fig. 23(a). The insulating samples with $m = 1$ and 2 show a magnetic transition with weak-ferromagnetic moments, which are induced by the rotations of IrO₆ octahedra about the [001] axis and the resultant DM interaction [Fig. 23(d)]. The intimate correlation between the metal-insulator transition and the appearance of magnetic order suggests that magnetism is essential for the occurrence of a metal-insulator transition with reducing m .

The nodal-line Dirac semimetallic state of SrIrO₃ can be potentially exploited as a platform for other correlated topological phases by the application of symmetry-breaking perturbations such as magnetic field and strain.¹⁷⁶ In particular, a variety of superlattice structures has been proposed to realize novel topologi-

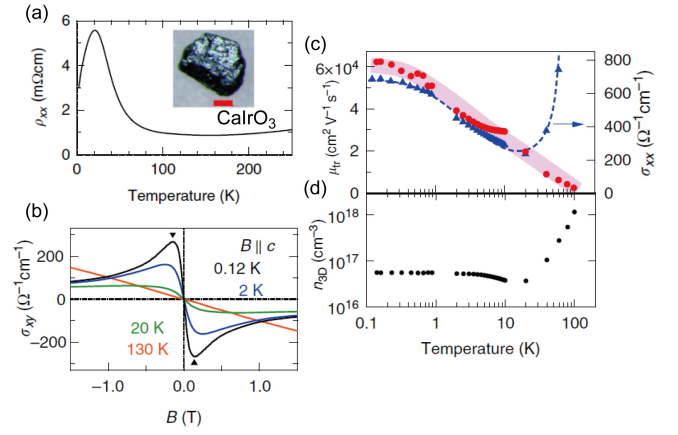


FIG. 22. Transport properties of orthorhombic perovskite CaIrO₃. (a) Temperature dependence of longitudinal resistivity ρ_{xx} . (b) Hall conductivity σ_{xy} as a function of magnetic field at several temperatures. (c), (d) Temperature dependence of carrier mobility μ_{tr} and carrier density n_{3D} , respectively. The huge mobility as large as 60,000 cm²/V·s is seen below 1 K. The figure is reproduced from Ref. [178], CC-BY-4.0 (<http://creativecommons.org/licenses/by/4.0/>).

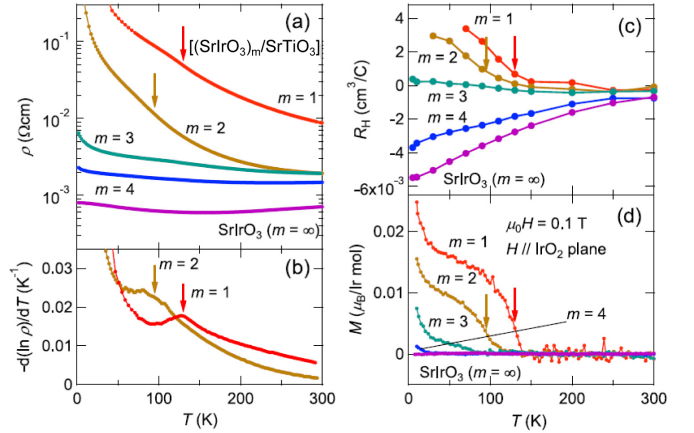


FIG. 23. Temperature dependent (a) resistivity $\rho(T)$, (b) $-d(\ln\rho)/dT$, (c) Hall constant R_H , and (d) in-plane magnetization $M(T)$ of (001) superlattice [(SrIrO₃)_m/SrTiO₃] with $m = 1, 2, 3, 4$ and ∞ . The figure is reproduced with permission from Ref. [179] (©2015 the American Physical Society).

cal phases. By introducing a staggered potential that breaks the mirror-symmetry, for example the (001) superlattice of [(SrIrO₃)/(SrRhO₃)], the appearance of a topological insulator phase is anticipated.¹⁷³ The superlattice of [(SrIrO₃)₂/(CaIrO₃)₂] has been predicted to be a topological semimetal hosting a double-helical surface state.¹⁸⁰

In addition to the (001) superlattices, a topological insulator phase was also predicted from fabricating a bilayer of SrIrO₃ along the [111] direction.^{181–183} In a bilayer of SrIrO₃, the IrO₆ octahedra form a buckled hon-

eycomb lattice. As in the celebrated graphene, electron hopping on a honeycomb lattice gives rise to Dirac bands. When a trigonal crystal field is incorporated, it opens a gap at the Dirac points, giving rise to a Z_2 topological insulator.¹⁸¹

In fact, the fabrication of a [111] oriented thin-film is technically challenging in perovskite oxides $A^{2+}B^{4+}O_3$, since the (111) surfaces, AO_3 or B planes, are polar, in contrast to the (001) surfaces of AO or BO_2 .¹⁸⁴ Additional difficulties arise from a size mismatch of $SrIrO_3$ with a standard substrate like $SrTiO_3$ and the stability of monoclinic $SrIrO_3$ with a hexagonal motif on a [111] substrate.¹⁸⁵ The stabilization of the orthorhombic phase by optimizing the A-site ion through Ca substitution for Sr is quite useful to overcome this difficulty. (111) superlattices of $[(Ca_{0.5}Sr_{0.5}IrO_3)_{2m}/(SrTiO_3)]$ with $m = 1, 2$ and 3 have been successfully fabricated.¹⁸⁶ In contrast to the prediction of a topological insulator, the (111) superlattices with $m \leq 3$ were found to be magnetic insulators and likely trivial. This again points to the importance of magnetism in the superlattices of iridates.¹⁸²

B. Potential topological semimetallic state in pyrochlore iridates

Since soon after the discovery of spin-orbit-entangled phases in iridates, the pyrochlore iridates $A_2Ir_2O_7$ (A: trivalent cation) have been attracting tremendous interest, as they provide a unique interplay between SOC, electron correlation and frustration. There have been a plethora of theoretical proposals for non-trivial topological phases, including Z_2 topological insulators,¹⁸⁷ topological Mott insulators,¹⁸⁸ Weyl semimetals,⁹⁷ and axion insulators.^{97,189}

The general trend for the electronic structure of pyrochlore iridates has been understood as follows.¹⁹⁰ When the on-site electron correlation U is weak, they show a semimetallic electronic structure. The semimetallic state may contain small pocket Fermi surfaces [Fig. 24(a)] or a quadratic band touching point at the Γ point near the Fermi energy [Fig. 24(b)], depending on the hopping parameters. By increasing the electron correlation, AIAO order of Ir magnetic moments takes place. When the original nonmagnetic state is a semimetal with quadratic band touching, the AIAO order splits the degenerate bands and gives rise to crossings of linearly-dispersing non-degenerate bands. The resultant semimetallic phase is a Weyl semimetal with nodes of opposite chiralities. There are 4 pairs of Weyl nodes along the [111] or equivalent directions in the Brillouin zone. When U is increased further, the Weyl nodes move to the high-symmetry point of the Brillouin zone and the distance between the pair of nodes increases. Eventually, the pair of Weyl nodes with different chiralities meets at the zone boundary and annihilates, which renders a gap over the whole Brillouin zone and makes the system a trivial AIAO antiferromagnetic insulator.

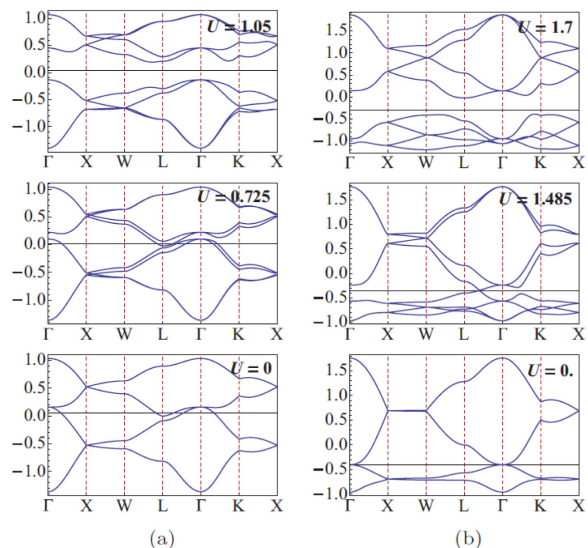


FIG. 24. Calculated band structures of pyrochlore iridate near Fermi energy with different on-site Hubbard repulsion U . The left and right columns show the results for the different magnitude of hopping parameters. The figure is taken with permission from Ref. [190] (©2013 the American Physical Society).

In real materials, the relative strength of U can be tuned effectively by changing the bandwidth of Ir $5d$ states. As described in Sec.III.C.2, the bandwidth is reduced by decreasing the ionic radius of the A-cation, r_A , i.e. changing the degree of trigonal distortion. Among the family of pyrochlore iridates $A_2Ir_2O_7$, $Pr_2Ir_2O_7$, which has the largest r_A , remains metallic down to the lowest temperature measured. $Pr_2Ir_2O_7$ shows a poor metallic behavior with a small carrier density of $\sim 10^{21} \text{ cm}^{-3}$.¹⁹¹ The ARPES measurement revealed that $Pr_2Ir_2O_7$ has a quadratic band-touching at the Γ point as shown in Fig. 25.¹⁹² In this nodal semimetallic state, the density of states near E_F increases steeply since $\text{DOS}(E) \propto \sqrt{E}$, which results in pronounced electron correlations and potentially leads to a non-Fermi liquid behavior.¹⁹³ Another interesting behavior of $Pr_2Ir_2O_7$ is that Pr^{3+} $4f$ moments do not show a long-range magnetic order, but instead a spin-liquid-like behavior.¹⁹⁴ A finite Hall conductivity was observed at zero magnetic field despite the absence of hysteresis in the magnetization curve, which has been discussed to originate from the chirality of the spin-liquid state.¹⁹⁵

With decreasing r_A , a temperature-driven metal-insulator transition is observed for $A = \text{Nd}, \text{Sm},$ and Eu . The metal-insulator transition accompanies the AIAO magnetic order of Ir $5d$ moments as discussed in Sec.III.C, and thus the low-temperature phase was expected as a possible realization of a Weyl semimetal. However, the presence of a charge gap has been seen at temperatures well below the magnetic ordering tem-

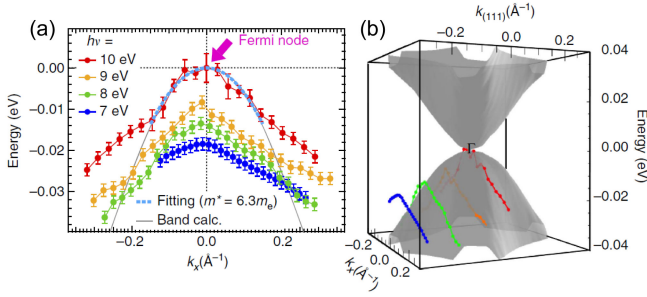


FIG. 25. Quadratic Fermi node of $\text{Pr}_2\text{Ir}_2\text{O}_7$ revealed by the ARPES measurement. (a) Energy dispersion along k_x direction measured with different incidence photon energies. (b) The ARPES data in the $k_x - k_{(111)}$ sheet superposed on the calculated band dispersion. The figure is reproduced from Ref. [192], CC-BY-4.0 (<http://creativecommons.org/licenses/by/4.0/>).

perature T_N for Ir 5d moments even in $\text{Nd}_2\text{Ir}_2\text{O}_7$,^{196,197} which is right next to $\text{Pr}_2\text{Ir}_2\text{O}_7$. This is incompatible with the Weyl semimetallic state. A Weyl semimetal phase might be realized only in the critical vicinity of a metal-insulator transition and therefore hidden. Fine tuning of the metal-insulator transition using pressure or doping may help approaching a Weyl semimetal. Indeed, suppression of the metal-insulator transition was observed by the application of pressure^{198,199} or by doping a small amount of Rh atoms onto the Ir site,¹⁹⁶ which may stabilize the Weyl semimetallic state.

Although the ground state of $\text{Nd}_2\text{Ir}_2\text{O}_7$ is unlikely to be a Weyl semimetal at ambient conditions, a drastic magnetic-field-induced change of transport properties was discovered, reflecting the modification of Nd^{3+} magnetic order.^{200,201} When a magnetic field is applied along the [001] direction, the AIAO order of Nd^{3+} 4f moments is switched into the 2-in-2-out configuration above ~ 10 T. Concomitantly, a drastic drop of resistivity was observed as shown in Fig. 26, indicating an insulator to semimetal transition by suppressing the AIAO order of Ir 5d electrons via the f - d magnetic exchange. The high-field semimetallic state has been proposed to be a nodal-line semimetal.^{200,202} On the other hand, an application of magnetic field along the [111] direction induces the 3-in-1-out order of Nd^{3+} moments, which is discussed to realize another Weyl semimetallic phase.²⁰²

The putative Weyl semimetallic state in pyrochlore iridates is expected to show characteristic features such as surface Fermi arcs and anomalous Hall effect (AHE). The AHE is associated with the fact that the Weyl nodes can be regarded as a source/sink of Berry curvature. In a bulk pyrochlore iridate, the anomalous Hall conductivity is canceled because of the cubic symmetry.²⁰³ However, in a strained thin-film, the cubic symmetry is broken and the emergence of an AHE has been predicted.²⁰⁴ Experimentally, such an AHE was indeed observed in thin-film

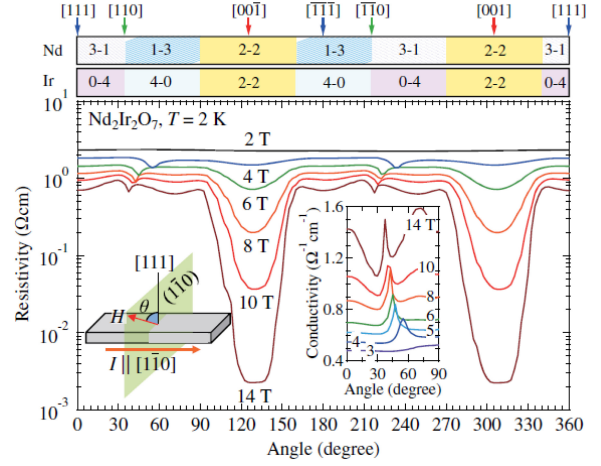


FIG. 26. Angle-dependent magnetoresistance in $\text{Nd}_2\text{Ir}_2\text{O}_7$. The tables on the top indicate the magnetic configuration of Nd and Ir sublattices such as AIAO (AOAI) order (0-4 and 4-0), 2-in-2-out configuration (2-2) and 3-in-1-out state (3-1 or 1-3), respectively. The figure is reproduced with permission from Ref. [200] (©2015 the American Physical Society).

pyrochlore iridates. For the $\text{Pr}_2\text{Ir}_2\text{O}_7$ thin-film, this was argued to arise from the strain-induced Weyl semimetallic state with a magnetic order at the surface/interface as well as the breaking of cubic-symmetry.²⁰⁵ The AHE was observed also in the insulating pyrochlores such as $\text{Eu}_2\text{Ir}_2\text{O}_7$ and $\text{Nd}_2\text{Ir}_2\text{O}_7$, but was attributed to spin-chirality²⁰⁶ or domain walls²⁰⁷ of AIAO magnetic order, rather than the anomalous conductivity from Weyl nodes.

C. Spin-orbit-coupled semimetal out of the competition with molecular orbital formation

A metallic state is realized also by carrier doping into spin-orbit-entangled Mott insulators. In particular, carrier-doping into Sr_2IrO_4 has been attempted intensively in the search for superconductivity, motivated by the cuprate physics, as discussed in Sec.III.A. A spin-orbit-coupled metallic state induced by carrier-doping was found also in the doped hyperkagome iridate $\text{Na}_4\text{Ir}_3\text{O}_8$. A sister compound $\text{Na}_3\text{Ir}_3\text{O}_8$, which shares the same hyperkagome sublattice of Ir atoms was synthesized.²⁰⁸ The chemical formula indicates that Ir has a valence state of $\text{Ir}^{4.33+}$, i.e. 1/3-hole doped state of the $\text{Na}_4\text{Ir}_3\text{O}_8$ Mott insulator.

Naively, we would expect the 1/3-hole-doped Mott insulator to be a correlated metal with a large Fermi surface. $\text{Na}_3\text{Ir}_3\text{O}_8$, as well as the sister compound $\text{Li}_3\text{Ir}_3\text{O}_8$,²⁰⁹ shows a metallic behavior, but turned out to be a semimetal with a small number of electrons and holes, rather than a large Fermi-surface metal.²⁰⁸ The first-principle calculations indicate that the semimetallic

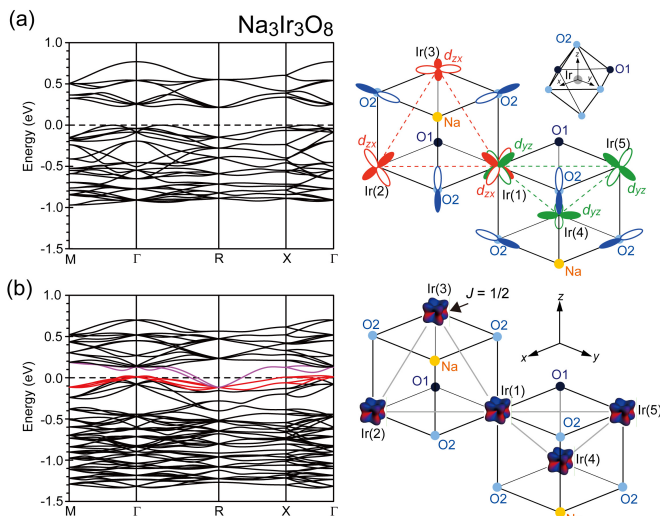


FIG. 27. Calculated band structure of $\text{Na}_3\text{Ir}_3\text{O}_8$. (a) Scalar relativistic band structure showing a band insulating state. The right panel illustrates the molecular orbital formation on the Ir hyperkagome lattice. (b) Relativistic band structure including SOC. The bands which form hole and electron pockets are colored in red and magenta, respectively. The right panel schematically represents the suppression of molecular orbital formation by SOC. The figures are reproduced from Ref. [208], CC-BY-4.0 (<http://creativecommons.org/licenses/by/4.0/>).

electronic structure is produced by an interplay of molecular orbital formation and SOC. The calculation without SOC yields a band insulator as the ground state of $\text{Na}_3\text{Ir}_3\text{O}_8$, despite the non-integer number of d -electrons per Ir atom. The band insulating state can be understood as the formation of Ir_3 trimer molecules with 14 d -electrons on the triangular unit of the hyperkagome lattice [Fig. 27(a)]. The incorporation of SOC suppresses the formation of molecular orbitals by orbital mixing. The conduction and valence bands made out of the molecular orbitals get broader and overlap, giving rise to a semimetallic state with small pockets of Fermi surface. Such a competition between molecular orbital formation and SOC is likely a common feature of $4d$ and $5d$ transition-metal oxides with spatially extended d -orbitals. Indeed, $J = 1/2$ magnets often switch into a dimerized state of transition-metal ions, which can be viewed as a molecular orbital formation, for example, in honeycomb-based iridates and in the ruthenium chloride under high pressure.^{210–213}

D. Spin-orbit-coupled metallic state in $\text{Cd}_2\text{Re}_2\text{O}_7$

The pyrochlore material $\text{Cd}_2\text{Re}_2\text{O}_7$ has received much attention in recent years due to the spontaneous breaking of inversion symmetry, and its impact on superconductivity below $T_c \sim 1$ K. The multitudinous experimental studies of this compound have been well reviewed in

Ref. [214], and we briefly discuss here the basic physical ideas.

The most popular theoretical framework for describing $\text{Cd}_2\text{Re}_2\text{O}_7$ is that of strongly spin-orbit-coupled metals with relatively weak electron-electron interactions.²¹⁵ Starting from the high-temperature metal with intact time-reversal and inversion symmetries, one can consider the possible Fermi-surface instabilities. These include phases in which inversion symmetry is spontaneously broken, while time-reversal symmetry remains intact, and the result is a deformation and splitting of the Fermi-surface into spin polarised bands, with momentum-dependent spin orientation (see Fig. 28). Many of these electronic order parameters couple to the lattice, and should therefore drive a structural phase transition. The instability that may be relevant to $\text{Cd}_2\text{Re}_2\text{O}_7$ results in a quadrupolar order parameter, and can be thought of as the electron analog of chiral nematic liquid crystals.²¹⁶

The inversion symmetry breaking instability may open up the possibility of unconventional, odd-parity, topological superconductivity in the vicinity of the associated quantum critical point.^{217,218} The superconductivity mediated by the fluctuations of the inversion-symmetry-breaking order parameter can be either pure p -wave or mixed s - and p -wave, where the s - and p -mixed state comes from distinct superconducting channels developing from the weakly-coupled, SOC-split bands (see Fig. 28). In the case that the p -wave channel is dominant, a topologically non-trivial state is expected, and the topological transition between the s - and p -wave dominated regions is particularly interesting due to the presence of unusual vortex defects associated with the enlarged symmetry.²¹⁸

Experimentally, an inversion-symmetry-breaking structural transition has been observed in $\text{Cd}_2\text{Re}_2\text{O}_7$ at $T_{s1} \approx 200$ K, while superconductivity sets in at $T_c \approx 1$ K.²¹⁴ Analysis of second-harmonic generation experiments has been used to tease apart the lattice and electronic changes at T_{s1} , and suggests that an inversion-symmetry-breaking electronic nematic phases is formed at the transition.²¹⁹ For lower temperatures, while at ambient pressure the superconductivity appears to be essentially s -wave, pressure can be used to tune the system, increasing both T_c and the upper critical field, B_{c2} , with the significant increase of the latter taken to indicate the enhancement of the p -wave channel.²¹⁴ While the agreement between theory and experiment is very encouraging, the experimental phase diagram as a function of both temperature and pressure is considerably more complicated than the theoretical predictions, and much work remains on both the theoretical and experimental fronts.

VII. CONCLUSION

Correlated electrons in the presence of strong SOC form a rich variety of localized and itinerant spin-orbit-

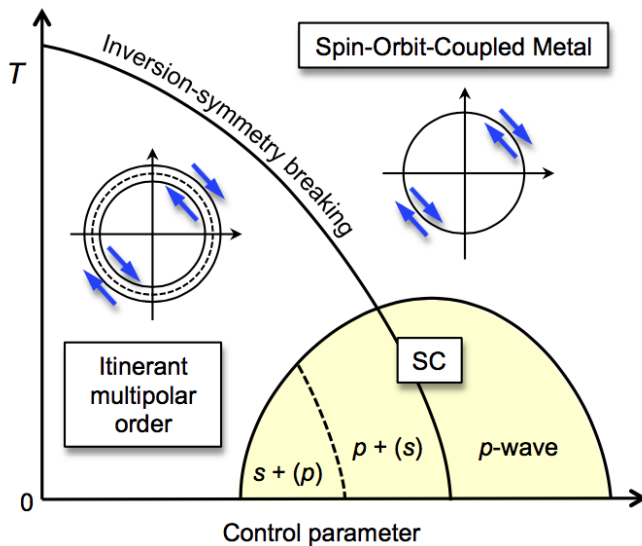


FIG. 28. Schematic theoretical phase diagram for spin-orbit-coupled metals. The breaking of inversion symmetry drives an itinerant multipolar-ordered phase with spin split bands, where the spin orientation is tied to the momentum.²¹⁵ As a function of a control parameter, such as pressure, a quantum critical point for inversion-symmetry breaking emerges. At around the quantum critical point, a dome-like superconducting phase may be anticipated. The superconducting dome consists of pure p -wave region and mixed s - and p -wave region. Exotic topological properties are expected when the p -wave pairing dominates.^{217,218} The figure is reproduced with permission from Ref. [214] (©2018 The Physical Society of Japan).

entangled phases in $4d$ and $5d$ transition metal compounds. Localized $4d^5$ and $5d^5$ systems with $J = 1/2$ pseudospins have been explored extensively in the last

decade, which has established the $4d$ and $5d$ transition metal oxides and related compounds as an emergent paradigm in the search for unprecedented quantum phases. The Kitaev model has been shown to be relevant in a family of d^5 $J = 1/2$ honeycomb magnets. Partly motivated by the $J = 1/2$ physics in the insulating d^5 systems, the research effort on $d^1 - d^4$ and itinerant systems has become quite active recently. Many attractive spin-orbit-entangled states are anticipated to emerge, including multipolar orderings, excitonic magnetism, a correlated topological insulator, and a topological superconductor. As seen in this review, their potential as a mine of novel electronic phases has not yet been explored fully, particularly for $d^1 - d^4$ and itinerant systems. Concepts have been put forward, but their realization requires the development of novel materials and approaches. Unusual behaviors have been observed in experiments, but understanding the physics behind them requires more elaborate and realistic theories. Besides, many yet unknown exotic phases likely remain hidden, and are waiting to be unveiled both theoretically and experimentally. We are convinced that the whole family of $4d$ and $5d$ correlated oxides and related compounds with strong SOC constitutes a rich mine of novel quantum phases and is worthy of further exploration.

ACKNOWLEDGMENT

T.T., A.S. and H.T. were supported by Alexander von Humboldt Foundation. J.Ch. acknowledges support by Czech Science Foundation (GAČR) under Project No. GA19-16937S. G.Kh. acknowledges support by the European Research Council under Advanced Grant 669550 (Com4Com).

- ¹ A. Abragam and B. Bleaney, *Electron Paramagnetic Resonance of Transition Ions* (Clarendon Press, Oxford, 1970).
- ² A. Takahashi and H. Shiba, *J. Phys. Soc. Jpn.* **69**, 3328 (2000).
- ³ R. Maezono and N. Nagaosa, *Phys. Rev. B* **62**, 11576 (2000).
- ⁴ J. van den Brink and D. I. Khomskii, *Phys. Rev. B* **63**, 140416(R) (2001).
- ⁵ J. H. M. Thornley, *Journal of Physics C: Solid State Physics* **1**, 1024 (1968).
- ⁶ G. L. Stamokostas and G. A. Fiete, *Phys. Rev. B* **97**, 085150 (2018).
- ⁷ K. I. Kugel and D. I. Khomskii, *Sov. Phys. Usp.* **25**, 231 (1982).
- ⁸ G. Khaliullin, *Phys. Rev. B* **64**, 212405 (2001).
- ⁹ G. Khaliullin and S. Okamoto, *Phys. Rev. B* **68**, 205109 (2003).
- ¹⁰ G. Khaliullin, *Prog. Theor. Phys. Suppl.* **160**, 155 (2005).
- ¹¹ J. Kanamori, *Journal of Applied Physics* **31**, S14 (1960).
- ¹² G. Chen, R. Pereira, and L. Balents, *Phys. Rev. B* **82**, 174440 (2010).
- ¹³ H. Liu and G. Khaliullin, *Phys. Rev. Lett.* **122**, 057203 (2019).
- ¹⁴ G. Jackeli and G. Khaliullin, *Phys. Rev. Lett.* **102**, 017205 (2009).
- ¹⁵ A. Kitaev, *Ann. Phys.* **321**, 2 (2006).
- ¹⁶ A. M. Glazer, *Acta Crystallographica Section B* **28**, 3384 (1972).
- ¹⁷ Y. G. Shi, Y. F. Guo, S. Yu, M. Arai, A. A. Belik, A. Sato, K. Yamaura, E. Takayama-Muromachi, H. F. Tian, H. X. Yang, J. Q. Li, T. Varga, J. F. Mitchell, and S. Okamoto, *Phys. Rev. B* **80**, 161104 (2009).
- ¹⁸ W. Bensch, H. W. Schmalle, and A. Reller, *Solid State Ionics* **43**, 171 (1990).
- ¹⁹ J. Longo, J. Kafalas, and R. Arnott, *Journal of Solid State Chemistry* **3**, 174 (1971).
- ²⁰ M. K. Crawford, M. A. Subramanian, R. L. Harlow, J. A. Fernandez-Baca, Z. R. Wang, and D. C. Johnston, *Phys. Rev. B* **49**, 9198 (1994).

- ²¹ O. Friedt, M. Braden, G. André, P. Adelman, S. Nakatsuji, and Y. Maeno, *Phys. Rev. B* **63**, 174432 (2001).
- ²² K. Momma and F. Izumi, *Journal of Applied Crystallography* **44**, 1272 (2011).
- ²³ R. Armstrong, *Physics Report* **57**, 343 (1980).
- ²⁴ M. Subramanian, G. Aravamudan, and G. Subba Rao, *Progress in Solid State Chemistry* **15**, 55 (1983).
- ²⁵ J. S. Gardner, M. J. P. Gingras, and J. E. Greedan, *Rev. Mod. Phys.* **82**, 53 (2010).
- ²⁶ Y. Moritomo, S. Xu, A. Machida, T. Katsufuji, E. Nishibori, M. Takata, M. Sakata, and S.-W. Cheong, *Phys. Rev. B* **63**, 144425 (2001).
- ²⁷ K. Matsuhira, M. Wakeshima, Y. Hinatsu, and S. Takagi, *Journal of the Physical Society of Japan* **80**, 094701 (2011).
- ²⁸ G. C. Mather, C. Dussarrat, J. Etourneau, and A. R. West, *J. Mater. Chem.* **10**, 2219 (2000).
- ²⁹ T. Takayama, A. Kato, R. Dinnebier, J. Nuss, H. Kono, L. S. I. Veiga, G. Fabbri, D. Haskel, and H. Takagi, *Phys. Rev. Lett.* **114**, 077202 (2015).
- ³⁰ K. A. Modic, T. E. Smidt, I. Kimchi, N. P. Breznay, A. Biffin, S. Choi, R. D. Johnson, R. Coldea, P. Watkins-Curry, G. T. McCandless, J. Y. Chan, F. Gandara, Z. Islam, A. Vishwanath, A. Shekhter, R. D. McDonald, and J. G. Analytis, *Nat. Commun.* **5**, 4203 (2014).
- ³¹ Y. Okamoto, M. Nohara, H. Aruga-Katori, and H. Takagi, *Phys. Rev. Lett.* **99**, 137207 (2007).
- ³² J. B. Goodenough, *Magnetism and the Chemical Bond* (Interscience Publ., New York, 1963).
- ³³ B. J. Kim, H. Jin, S. J. Moon, J.-Y. Kim, B.-G. Park, C. S. Leem, J. Yu, T. W. Noh, C. Kim, S.-J. Oh, J.-H. Park, V. Durairaj, G. Cao, and E. Rotenberg, *Phys. Rev. Lett.* **101**, 076402 (2008).
- ³⁴ B. J. Kim, H. Ohsumi, T. Komesu, S. Sakai, T. Morita, H. Takagi, and T. Arima, *Science* **323**, 1329 (2009).
- ³⁵ Q. Huang, J. L. Soubeyroux, O. Chmaissem, I. Natali Sora, A. Santoro, R. J. Cava, J. J. Krajewski, and W. F. Peck Jr., *J. Solid State Chem.* **112**, 355 (1994).
- ³⁶ J. H. Van Vleck, *Phys. Rev.* **52**, 1178 (1937).
- ³⁷ S. Fujiyama, H. Ohsumi, T. Komesu, J. Matsuno, B. J. Kim, M. Takata, T. Arima, and H. Takagi, *Phys. Rev. Lett.* **108**, 247212 (2012).
- ³⁸ J. Kim, D. Casa, M. H. Upton, T. Gog, Y.-J. Kim, J. F. Mitchell, M. van Veenendaal, M. Daghofer, J. van den Brink, G. Khaliullin, and B. J. Kim, *Phys. Rev. Lett.* **108**, 177003 (2012).
- ³⁹ J. Porras, J. Bertinshaw, H. Liu, G. Khaliullin, N. H. Sung, J.-W. Kim, S. Francoual, P. Steffens, G. Deng, M. M. Sala, A. Efimenko, A. Said, D. Casa, X. Huang, T. Gog, J. Kim, B. Keimer, and B. J. Kim, *Phys. Rev. B* **99**, 085125 (2019).
- ⁴⁰ J. Kim, M. Daghofer, A. H. Said, T. Gog, J. van den Brink, G. Khaliullin, and B. J. Kim, *Nature Comm.* **5**, 4453 (2014).
- ⁴¹ H. Gretarsson, N. Sung, J. Porras, J. Bertinshaw, C. Dietl, J. A. Bruin, A. Bangura, Y. Kim, R. Dinnebier, J. Kim, A. Al-Zein, M. M. Sala, M. Krisch, M. L. Tacon, B. Keimer, and B. Kim, *Phys. Rev. Lett.* **117**, 107001 (2016).
- ⁴² X. Liu, M. P. M. Dean, Z. Y. Meng, M. H. Upton, T. Qi, T. Gog, Y. Cao, J. Q. Lin, D. Meyers, H. Ding, G. Cao, and J. P. Hill, *Phys. Rev. B* **93**, 241102(R) (2016).
- ⁴³ Y. K. Kim, O. Krupin, J. D. Denlinger, A. Bostwick, E. Rotenberg, Q. Zhao, J. F. Mitchell, J. W. Allen, and B. J. Kim, *Science* **345**, 187 (2014).
- ⁴⁴ Y. K. Kim, N. H. Sung, J. D. Denlinger, and B. J. Kim, *Nature Phys.* **12**, 37 (2016).
- ⁴⁵ Y. J. Yan, M. Q. Ren, H. C. Xu, B. P. Xie, R. Tao, H. Y. Choi, N. Lee, Y. J. Choi, T. Zhang, and D. L. Feng, *Phys. Rev. X* **5**, 041018 (2015).
- ⁴⁶ C. Lu, S. Dong, A. Quindeau, D. Preziosi, N. Hu, and M. Alexe, *Phys. Rev. B* **91**, 104401 (2015).
- ⁴⁷ J. Ravichandran, C. R. Serrao, D. K. Efetov, D. Yi, Y. S. Oh, S.-W. Cheong, R. Ramesh, and P. Kim, *J. Phys. Condens. Matter* **28**, 505304 (2016).
- ⁴⁸ J. Bertinshaw, Y. K. Kim, G. Khaliullin, and B. J. Kim, *Annu. Rev. Condens. Matter Phys.* **10**, 315 (2019).
- ⁴⁹ S. J. Moon, H. Jin, K. W. Kim, W. S. Choi, Y. S. Lee, J. Yu, G. Cao, A. Sumi, H. Funakubo, C. Bernhard, and T. W. Noh, *Phys. Rev. Lett.* **101**, 226402 (2008).
- ⁵⁰ J. W. Kim, Y. Choi, J. Kim, J. F. Mitchell, G. Jackeli, M. Daghofer, J. van den Brink, G. Khaliullin, and B. J. Kim, *Phys. Rev. Lett.* **109**, 037204 (2012).
- ⁵¹ J. Kim, A. H. Said, D. Casa, M. H. Upton, T. Gog, M. Daghofer, G. Jackeli, J. van den Brink, G. Khaliullin, and B. J. Kim, *Phys. Rev. Lett.* **109**, 157402 (2012).
- ⁵² M. M. Sala, V. Schnells, S. Boseggia, L. Simonelli, A. Al-Zein, J. G. Vale, L. Paolasini, E. C. Hunter, R. S. Perry, D. Prabhakaran, A. T. Boothroyd, M. Krisch, G. Monaco, H. M. Rønnow, D. F. McMorrow, and F. Mila, *Phys. Rev. B* **92**, 024405 (2015).
- ⁵³ J. G. Rau, E. K.-H. Lee, and H.-Y. Kee, *Annu. Rev. Condens. Matter Phys.* **7**, 195 (2016).
- ⁵⁴ S. M. Winter, A. A. Tsirlin, M. Daghofer, J. van den Brink, Y. Singh, P. Gegenwart, and R. Valentí, *J. Phys.: Condens. Matter* **29**, 493002 (2017).
- ⁵⁵ S. Trebst, arXiv e-prints, arXiv:1701.07056.
- ⁵⁶ M. Hermanns, I. Kimchi, and J. Knolle, *Annu. Rev. Condens. Matter Phys.* **9**, 17 (2018).
- ⁵⁷ H. Takagi, T. Takayama, G. Jackeli, G. Khaliullin, and S. E. Nagler, *Nature Reviews Physics* **1**, 264 (2019).
- ⁵⁸ Y. Motome and J. Nasu, *J. Phys. Soc. Jpn.* **89**, 012002 (2020).
- ⁵⁹ V. M. Katukuri, S. Nishimoto, V. Yushankhai, A. Stoyanova, H. Kandpal, S. Choi, R. Coldea, I. Rousochatzakis, L. Hozoi, and J. van den Brink, *New J. Phys.* **16**, 013056 (2014).
- ⁶⁰ J. G. Rau, E. K.-H. Lee, and H.-Y. Kee, *Phys. Rev. Lett.* **112**, 077204 (2014).
- ⁶¹ J. G. Rau and H.-Y. Kee, arXiv e-prints, arXiv:1408.4811.
- ⁶² S. M. Winter, Y. Li, H. O. Jeschke, and R. Valentí, *Phys. Rev. B* **93**, 214431 (2016).
- ⁶³ J. Chaloupka and G. Khaliullin, *Phys. Rev. B* **92**, 024413 (2015).
- ⁶⁴ H. Liu and G. Khaliullin, *Phys. Rev. B* **97**, 014407 (2018).
- ⁶⁵ R. Sano, Y. Kato, and Y. Motome, *Phys. Rev. B* **97**, 014408 (2018).
- ⁶⁶ H. Liu, J. Chaloupka, and G. Khaliullin, *Phys. Rev. Lett.* **125**, 047201 (2020).
- ⁶⁷ G. Khaliullin, W. Koshibae, and S. Maekawa, *Phys. Rev. Lett.* **93**, 176401 (2004).
- ⁶⁸ T. Hyart, A. R. Wright, G. Khaliullin, and B. Rosenow, *Phys. Rev. B* **85**, 140510(R) (2012).
- ⁶⁹ Y.-Z. You, I. Kimchi, and A. Vishwanath, *Phys. Rev. B* **86**, 085145 (2012).
- ⁷⁰ S. Okamoto, *Phys. Rev. Lett.* **110**, 066403 (2013).
- ⁷¹ G. Chen and L. Balents, *Phys. Rev. B* **78**, 094403 (2008).

- ⁷² A. C. Shockley, F. Bert, J.-C. Orain, Y. Okamoto, and P. Mendels, *Phys. Rev. Lett.* **115**, 047201 (2015).
- ⁷³ R. Dally, T. Hogan, A. Amato, H. Luetkens, C. Baines, J. Rodriguez-Rivera, M. J. Graf, and S. D. Wilson, *Phys. Rev. Lett.* **113**, 247601 (2014).
- ⁷⁴ H. Zheng, J. Zhang, C. C. Stoumpos, Y. Ren, Y.-S. Chen, R. Dally, S. D. Wilson, Z. Islam, and J. F. Mitchell, *Phys. Rev. Materials* **2**, 043403 (2018).
- ⁷⁵ J. M. Hopkinson, S. V. Isakov, H.-Y. Kee, and Y. B. Kim, *Phys. Rev. Lett.* **99**, 037201 (2007).
- ⁷⁶ Y. Zhou, P. A. Lee, T.-K. Ng, and F.-C. Zhang, *Phys. Rev. Lett.* **101**, 197201 (2008).
- ⁷⁷ M. J. Lawler, H.-Y. Kee, Y. B. Kim, and A. Vishwanath, *Phys. Rev. Lett.* **100**, 227201 (2008).
- ⁷⁸ M. J. Lawler, A. Paramakanti, Y. B. Kim, and L. Balents, *Phys. Rev. Lett.* **101**, 197202 (2008).
- ⁷⁹ M. R. Norman and T. Micklitz, *Phys. Rev. B* **81**, 024428 (2010).
- ⁸⁰ I. Kimchi and A. Vishwanath, *Phys. Rev. B* **89**, 014414 (2014).
- ⁸¹ T. Micklitz and M. R. Norman, *Phys. Rev. B* **81**, 174417 (2010).
- ⁸² R. Shindou, *Phys. Rev. B* **93**, 094419 (2016).
- ⁸³ T. Mizoguchi, K. Hwang, E. K.-H. Lee, and Y. B. Kim, *Phys. Rev. B* **94**, 064416 (2016).
- ⁸⁴ H. Kuriyama, J. Matsuno, S. Niitaka, M. Uchida, D. Hashizume, A. Nakao, K. Sugimoto, H. Ohsumi, M. Takata, and H. Takagi, *Applied Physics Letters* **96**, 182103 (2010).
- ⁸⁵ S. Onoda and F. Ishii, *Phys. Rev. Lett.* **122**, 067201 (2019).
- ⁸⁶ D. Yanagishima and Y. Maeno, *Journal of the Physical Society of Japan* **70**, 2880 (2001).
- ⁸⁷ K. Matsuhira, M. Wakeshima, R. Nakanishi, T. Yamada, A. Nakamura, W. Kawano, S. Takagi, and Y. Hinatsu, *Journal of the Physical Society of Japan* **76**, 043706 (2007).
- ⁸⁸ H. Shinaoka, S. Hoshino, M. Troyer, and P. Werner, *Phys. Rev. Lett.* **115**, 156401 (2015).
- ⁸⁹ L. Hozoi, H. Gretarsson, J. P. Clancy, B.-G. Jeon, B. Lee, K. H. Kim, V. Yushankhai, P. Fulde, D. Casa, T. Gog, J. Kim, A. H. Said, M. H. Upton, Y.-J. Kim, and J. van den Brink, *Phys. Rev. B* **89**, 115111 (2014).
- ⁹⁰ A. Krajewska, T. Takayama, R. Dinnebier, A. Yaresko, K. Ishii, M. Isobe, and H. Takagi, *Phys. Rev. B* **101**, 121101 (2020).
- ⁹¹ R. Moessner and J. T. Chalker, *Phys. Rev. Lett.* **80**, 2929 (1998).
- ⁹² M. Elhajal, B. Canals, R. Sunyer, and C. Lacroix, *Phys. Rev. B* **71**, 094420 (2005).
- ⁹³ H. Sagayama, D. Uematsu, T. Arima, K. Sugimoto, J. J. Ishikawa, E. O'Farrell, and S. Nakatsuji, *Phys. Rev. B* **87**, 100403 (2013).
- ⁹⁴ C. Donnerer, M. C. Rahn, M. M. Sala, J. G. Vale, D. Pincini, J. Strempler, M. Krisch, D. Prabhakaran, A. T. Boothroyd, and D. F. McMorrow, *Phys. Rev. Lett.* **117**, 037201 (2016).
- ⁹⁵ S. H. Chun, B. Yuan, D. Casa, J. Kim, C.-Y. Kim, Z. Tian, Y. Qiu, S. Nakatsuji, and Y.-J. Kim, *Phys. Rev. Lett.* **120**, 177203 (2018).
- ⁹⁶ E. K.-H. Lee, S. Bhattacharjee, and Y. B. Kim, *Phys. Rev. B* **87**, 214416 (2013).
- ⁹⁷ X. Wan, A. M. Turner, A. Vishwanath, and S. Y. Savrasov, *Phys. Rev. B* **83**, 205101 (2011).
- ⁹⁸ G. Khaliullin, *Phys. Rev. Lett.* **111**, 197201 (2013).
- ⁹⁹ O. N. Meetei, W. S. Cole, M. Randeria, and N. Trivedi, *Phys. Rev. B* **91**, 054412 (2015).
- ¹⁰⁰ T. Giamarchi, C. Rüegg, and O. Tchernyshyov, *Nature Phys.* **4**, 198 (2008).
- ¹⁰¹ M. Vojta, *Rep. Prog. Phys.* **81**, 064501 (2018).
- ¹⁰² A. Jain, M. Krautloher, J. Porras, G. H. Ryu, D. P. Chen, D. L. Abernathy, J. T. Park, A. Ivanov, J. Chaloupka, G. Khaliullin, B. Keimer, and B. J. Kim, *Nature Phys.* **13**, 633 (2017).
- ¹⁰³ S.-M. Souliou, J. Chaloupka, G. Khaliullin, G. Ryu, A. Jain, B. J. Kim, M. L. Tacon, and B. Keimer, *Phys. Rev. Lett.* **119**, 067201 (2017).
- ¹⁰⁴ S. Nakatsuji, S. Ikeda, and Y. Maeno, *J. Phys. Soc. Jpn.* **66**, 1868 (1997).
- ¹⁰⁵ S. Nakatsuji and Y. Maeno, *Phys. Rev. Lett.* **84**, 2666 (2000).
- ¹⁰⁶ C. S. Alexander, G. Cao, V. Dobrosavljevic, S. McCall, J. E. Crow, E. Lochner, and R. P. Guertin, *Phys. Rev. B* **60**, R8422 (1999).
- ¹⁰⁷ G. Cao, S. McCall, M. Shepard, J. E. Crow, and R. P. Guertin, *Phys. Rev. B* **56**, R2916 (1997).
- ¹⁰⁸ M. Braden, G. André, S. Nakatsuji, and Y. Maeno, *Phys. Rev. B* **58**, 847 (1998).
- ¹⁰⁹ T. Mizokawa, L. H. Tjeng, G. A. Sawatzky, G. Ghiringhelli, O. Tjernberg, N. B. Brookes, H. Fukazawa, S. Nakatsuji, and Y. Maeno, *Phys. Rev. Lett.* **87**, 077202 (2001).
- ¹¹⁰ C. Rüegg, N. Cavadini, A. Furrer, H.-U. Güdel, K. Krämer, H. Mutka, A. Wildes, K. Habicht, and P. Vorderwisch, *Nature* **423**, 62 (2003).
- ¹¹¹ C. Rüegg, B. Normand, M. Matsumoto, A. Furrer, D. F. McMorrow, K. W. Krämer, H.-U. Güdel, S. N. Gvasaliya, H. Mutka, and M. Boehm, *Phys. Rev. Lett.* **100**, 205701 (2008).
- ¹¹² D. Podolsky, A. Auerbach, and D. P. Arovas, *Phys. Rev. B* **84**, 174522 (2011).
- ¹¹³ F. Rose, F. Léonard, and N. Dupuis, *Phys. Rev. B* **91**, 224501 (2015).
- ¹¹⁴ T. Dey, A. Maljuk, D. V. Efremov, O. Kataeva, S. Gass, C. G. F. Blum, F. Steckel, D. Gruner, T. Ritschel, A. U. B. Wolter, J. Geck, C. Hess, K. Koepf, J. van den Brink, S. Wurmehl, and B. Büchner, *Phys. Rev. B* **93**, 014434 (2016).
- ¹¹⁵ N. R. Davies, C. V. Topping, H. Jacobsen, A. J. Princep, F. K. K. Kirschner, M. C. Rahn, M. Bristow, J. G. Vale, I. da Silva, P. J. Baker, C. J. Sahle, Y.-F. Guo, D.-Y. Yan, Y.-G. Shi, S. J. Blundell, D. F. McMorrow, and A. T. Boothroyd, *Phys. Rev. B* **99**, 174442 (2019).
- ¹¹⁶ B. Yuan, J. P. Clancy, A. M. Cook, C. M. Thompson, J. Greedan, G. Cao, B. C. Jeon, T. W. Noh, M. H. Upton, D. Casa, T. Gog, A. Paramakanti, and Y.-J. Kim, *Phys. Rev. B* **95**, 235114 (2017).
- ¹¹⁷ S. Fuchs, T. Dey, G. Aslan-Cansever, A. Maljuk, S. Wurmehl, B. Büchner, and V. Kataev, *Phys. Rev. Lett.* **120**, 237204 (2018).
- ¹¹⁸ P. S. Anisimov, F. Aust, G. Khaliullin, and M. Daghofer, *Phys. Rev. Lett.* **122**, 177201 (2019).
- ¹¹⁹ J. Chaloupka and G. Khaliullin, *Phys. Rev. B* **100**, 224413 (2019).
- ¹²⁰ Z. Nussinov and J. van den Brink, *Rev. Mod. Phys.* **87**, 1 (2015).
- ¹²¹ S. A. J. Kimber, C. D. Ling, D. J. P. Morris, A. Chemseddine, P. F. Henry, and D. N. Argyriou, *J. Mater. Chem.*

- 20**, 8021 (2010).
- ¹²² R. Kumar, T. Dey, P. M. Ette, K. Ramesha, A. Chakraborty, I. Dasgupta, J. C. Orain, C. Baines, S. Tóth, A. Shahee, S. Kundu, M. Prinz-Zwick, A. A. Gippius, N. Büttgen, P. Gegenwart, and A. V. Mahajan, *Phys. Rev. B* **99**, 054417 (2019).
- ¹²³ T. Takayama *et al.* (unpublished).
- ¹²⁴ Y. Miura, Y. Yasui, M. Sato, N. Igawa, and K. Kakurai, *J. Phys. Soc. Jpn.* **76**, 033705 (2007).
- ¹²⁵ G. Jackeli and D. I. Khomskii, *Phys. Rev. Lett.* **100**, 147203 (2008).
- ¹²⁶ S. A. J. Kimber, I. I. Mazin, J. Shen, H. O. Jeschke, S. V. Streltsov, D. N. Argyriou, R. Valentí, and D. I. Khomskii, *Phys. Rev. B* **89**, 081408(R) (2014).
- ¹²⁷ J. Chaloupka and G. Khaliullin, *Phys. Rev. Lett.* **116**, 017203 (2016).
- ¹²⁸ G. Cao, S. McCall, V. Dobrosavljevic, C. S. Alexander, J. E. Crow, and R. P. Guertin, *Phys. Rev. B* **61**, R5053(R) (2000).
- ¹²⁹ G. Cao, C. S. Alexander, S. McCall, J. E. Crow, and R. P. Guertin, *J. Magn. Magn. Mater.* **226-230**, 235 (2001).
- ¹³⁰ F. Nakamura, M. Sakaki, Y. Yamanaka, S. Tamaru, T. Suzuki, and Y. Maeno, *Sci. Rep.* **3**, 2536 (2013).
- ¹³¹ H. Boschker, T. Harada, T. Asaba, R. Ashoori, A. Boris, H. Hilgenkamp, C. Hughes, M. Holtz, L. Li, D. Muller, H. Nair, P. Reith, X. R. Wang, D. Schlom, A. Soukiassian, and J. Mannhart, *Phys. Rev. X* **9**, 011027 (2019).
- ¹³² H. Nobukane, K. Yanagihara, Y. Kunisada, Y. Ogasawara, K. Isono, K. Nomura, K. Tanahashi, T. Nomura, T. Akiyama, and S. Tanda, *Sci. Rep.* **10**, 3462 (2020).
- ¹³³ A. Andreev and I. Grishchuk, *JETP* **87**, 467 (1984).
- ¹³⁴ N. Shannon, T. Momoi, and P. Sindzingre, *Phys. Rev. Lett.* **96**, 027213 (2006).
- ¹³⁵ Y. Kuramoto, H. Kusunose, and A. Kiss, *Journal of the Physical Society of Japan* **78**, 072001 (2009).
- ¹³⁶ P. Santini, S. Carretta, G. Amoretti, R. Caciuffo, N. Magnani, and G. H. Lander, *Rev. Mod. Phys.* **81**, 807 (2009).
- ¹³⁷ D. Hirai and Z. Hiroi, *Journal of the Physical Society of Japan* **88**, 064712 (2019).
- ¹³⁸ G. Chen, R. Pereira, and L. Balents, *Phys. Rev. B* **82**, 174440 (2010).
- ¹³⁹ M. Blume and Y. Hsieh, *Journal of Applied Physics* **40**, 1249 (1969).
- ¹⁴⁰ H. H. Chen and P. M. Levy, *Phys. Rev. Lett.* **27**, 1383 (1971).
- ¹⁴¹ N. Papanicolaou, *Nuclear Physics B* **305**, 367 (1988).
- ¹⁴² H. Ishikawa, T. Takayama, R. K. Kremer, J. Nuss, R. Dinnebier, K. Kitagawa, K. Ishii, and H. Takagi, *Phys. Rev. B* **100**, 045142 (2019).
- ¹⁴³ A. S. Erickson, S. Misra, G. J. Miller, R. R. Gupta, Z. Schlesinger, W. A. Harrison, J. M. Kim, and I. R. Fisher, *Phys. Rev. Lett.* **99**, 016404 (2007).
- ¹⁴⁴ L. Lu, M. Song, W. Liu, A. P. Reyes, P. Kuhns, H. O. Lee, I. R. Fisher, and V. F. Mitrović, *Nature Communications* **8**, 14407 EP (2017).
- ¹⁴⁵ K. Willa, R. Willa, U. Welp, I. R. Fisher, A. Rydh, W.-K. Kwok, and Z. Islam, *Phys. Rev. B* **100**, 041108 (2019).
- ¹⁴⁶ C. A. Marjerrison, C. M. Thompson, G. Sala, D. D. Maharaj, E. Kermarrec, Y. Cai, A. M. Hallas, M. N. Wilson, T. J. S. Munsie, G. E. Granroth, R. Flacau, J. E. Greedan, B. D. Gaulin, and G. M. Luke, *Inorganic Chemistry* **55**, 10701 (2016).
- ¹⁴⁷ D. Hirai, H. Sagayama, S. Gao, H. Ohsumi, G. Chen, T.-h. Arima, and Z. Hiroi, *Phys. Rev. Research* **2**, 022063 (2020).
- ¹⁴⁸ G. Chen and L. Balents, *Phys. Rev. B* **84**, 094420 (2011).
- ¹⁴⁹ G. Jackeli and G. Khaliullin, *Phys. Rev. Lett.* **103**, 067205 (2009).
- ¹⁵⁰ H. D. Zhou, B. S. Conner, L. Balicas, and C. R. Wiebe, *Phys. Rev. Lett.* **99**, 136403 (2007).
- ¹⁵¹ H. D. Zhou, Y. J. Jo, J. Fiore Carpino, G. J. Munoz, C. R. Wiebe, J. G. Cheng, F. Rivadulla, and D. T. Adroja, *Phys. Rev. B* **81**, 212401 (2010).
- ¹⁵² J. Teyssier, R. Viennois, E. Giannini, R. M. Eremina, A. Günther, J. Deisenhofer, M. V. Eremin, and D. van der Marel, *Phys. Rev. B* **84**, 205130 (2011).
- ¹⁵³ J. Teyssier, E. Giannini, A. Stucky, R. Černý, M. V. Eremin, and D. van der Marel, *Phys. Rev. B* **93**, 125138 (2016).
- ¹⁵⁴ A. Paramekanti, D. D. Maharaj, and B. D. Gaulin, *Phys. Rev. B* **101**, 054439 (2020).
- ¹⁵⁵ D. D. Maharaj, G. Sala, M. B. Stone, E. Kermarrec, C. Ritter, F. Fauth, C. A. Marjerrison, J. E. Greedan, A. Paramekanti, and B. D. Gaulin, *Phys. Rev. Lett.* **124**, 087206 (2020).
- ¹⁵⁶ C. M. Thompson, J. P. Carlo, R. Flacau, T. Aharen, I. A. Leahy, J. R. Pollicemi, T. J. S. Munsie, T. Medina, G. M. Luke, J. Munevar, S. Cheung, T. Goko, Y. J. Uemura, and J. E. Greedan, *Journal of Physics: Condensed Matter* **26**, 306003 (2014).
- ¹⁵⁷ C. A. Marjerrison, C. M. Thompson, A. Z. Sharma, A. M. Hallas, M. N. Wilson, T. J. S. Munsie, R. Flacau, C. R. Wiebe, B. D. Gaulin, G. M. Luke, and J. E. Greedan, *Phys. Rev. B* **94**, 134429 (2016).
- ¹⁵⁸ M. A. de Vries, A. C. McLaughlin, and J.-W. G. Bos, *Phys. Rev. Lett.* **104**, 177202 (2010).
- ¹⁵⁹ T. Aharen, J. E. Greedan, C. A. Bridges, A. A. Aczel, J. Rodriguez, G. MacDougall, G. M. Luke, T. Imai, V. K. Michaelis, S. Kroeker, H. Zhou, C. R. Wiebe, and L. M. D. Cranswick, *Phys. Rev. B* **81**, 224409 (2010).
- ¹⁶⁰ J. P. Carlo, J. P. Clancy, T. Aharen, Z. Yamani, J. P. C. Ruff, J. J. Wagman, G. J. Van Gastel, H. M. L. Noad, G. E. Granroth, J. E. Greedan, H. A. Dabkowska, and B. D. Gaulin, *Phys. Rev. B* **84**, 100404 (2011).
- ¹⁶¹ M. A. de Vries, J. O. Piatek, M. Misk, J. S. Lord, H. M. Rønnow, and J.-W. G. Bos, *New Journal of Physics* **15**, 043024 (2013).
- ¹⁶² J. Romhányi, L. Balents, and G. Jackeli, *Phys. Rev. Lett.* **118**, 217202 (2017).
- ¹⁶³ J. Greedan, M. Sato, X. Yan, and F. Razavi, *Solid State Communications* **59**, 895 (1986).
- ¹⁶⁴ H. Shinaoka, Y. Motome, T. Miyake, and S. Ishibashi, *Phys. Rev. B* **88**, 174422 (2013).
- ¹⁶⁵ A. Smerald and G. Jackeli, *Phys. Rev. Lett.* **122**, 227202 (2019).
- ¹⁶⁶ H. Shinaoka, Y. Motome, T. Miyake, S. Ishibashi, and P. Werner, *Journal of Physics: Condensed Matter* **31**, 323001 (2019).
- ¹⁶⁷ H. J. Silverstein, K. Fritsch, F. Flicker, A. M. Hallas, J. S. Gardner, Y. Qiu, G. Ehlers, A. T. Savici, Z. Yamani, K. A. Ross, B. D. Gaulin, M. J. P. Gingras, J. A. M. Paddison, K. Foyevtsova, R. Valenti, F. Hawthorne, C. R. Wiebe, and H. D. Zhou, *Phys. Rev. B* **89**, 054433 (2014).
- ¹⁶⁸ P. M. M. Thygesen, J. A. M. Paddison, R. Zhang, K. A. Beyer, K. W. Chapman, H. Y. Playford, M. G. Tucker, D. A. Keen, M. A. Hayward, and A. L. Goodwin, *Phys. Rev. Lett.* **118**, 067201 (2017).

- ¹⁶⁹ M. J. P. Gingras, C. V. Stager, N. P. Raju, B. D. Gaulin, and J. E. Greedan, *Phys. Rev. Lett.* **78**, 947 (1997).
- ¹⁷⁰ K. Mitsumoto, C. Hotta, and H. Yoshino, *Phys. Rev. Lett.* **124**, 087201 (2020).
- ¹⁷¹ J. G. Zhao, L. X. Yang, Y. Yu, F. Y. Li, R. C. Yu, Z. Fang, L. C. Chen, and C. Q. Jin, *Journal of Applied Physics* **103**, 103706 (2008).
- ¹⁷² Y. F. Nie, P. D. C. King, C. H. Kim, M. Uchida, H. I. Wei, B. D. Faeth, J. P. Ruf, J. P. C. Ruff, L. Xie, X. Pan, C. J. Fennie, D. G. Schlom, and K. M. Shen, *Phys. Rev. Lett.* **114**, 016401 (2015).
- ¹⁷³ J.-M. Carter, V. V. Shankar, M. A. Zeb, and H.-Y. Kee, *Phys. Rev. B* **85**, 115105 (2012).
- ¹⁷⁴ M. A. Zeb and H.-Y. Kee, *Phys. Rev. B* **86**, 085149 (2012).
- ¹⁷⁵ Y. Chen, H.-S. Kim, and H.-Y. Kee, *Phys. Rev. B* **93**, 155140 (2016).
- ¹⁷⁶ Y. Chen, Y.-M. Lu, and H.-Y. Kee, *Nature Communications* **6**, 6593 (2015).
- ¹⁷⁷ T. Takayama, A. N. Yaresko, and H. Takagi, *Journal of Physics: Condensed Matter* **31**, 074001 (2018).
- ¹⁷⁸ J. Fujioka, R. Yamada, M. Kawamura, S. Sakai, M. Hiramaya, R. Arita, T. Okawa, D. Hashizume, M. Hoshino, and Y. Tokura, *Nature Communications* **10**, 362 (2019).
- ¹⁷⁹ J. Matsuno, K. Ihara, S. Yamamura, H. Wadati, K. Ishii, V. V. Shankar, H.-Y. Kee, and H. Takagi, *Phys. Rev. Lett.* **114**, 247209 (2015).
- ¹⁸⁰ C. Fang, L. Lu, J. Liu, and L. Fu, *Nature Physics* **12**, 936 (2016).
- ¹⁸¹ D. Xiao, W. Zhu, Y. Ran, N. Nagaosa, and S. Okamoto, *Nature Communications* **2**, 596 (2011).
- ¹⁸² S. Okamoto and D. Xiao, *Journal of the Physical Society of Japan* **87**, 041006 (2018).
- ¹⁸³ J. L. Lado, V. Pardo, and D. Baldomir, *Phys. Rev. B* **88**, 155119 (2013).
- ¹⁸⁴ T. J. Anderson, S. Ryu, H. Zhou, L. Xie, J. P. Podkaminer, Y. Ma, J. Irwin, X. Q. Pan, M. S. Rzchowski, and C. B. Eom, *Applied Physics Letters* **108**, 151604 (2016).
- ¹⁸⁵ A. Sumi, Y. Kim, N. Oshima, K. Akiyama, K. Saito, and H. Funakubo, *Thin Solid Films* **486**, 182 (2005).
- ¹⁸⁶ D. Hirai, J. Matsuno, and H. Takagi, *APL Materials* **3**, 041508 (2015).
- ¹⁸⁷ H.-M. Guo and M. Franz, *Phys. Rev. Lett.* **103**, 206805 (2009).
- ¹⁸⁸ D. Pesin and L. Balents, *Nat. Phys.* **6**, 376 (2010).
- ¹⁸⁹ A. Go, W. Witzczak-Krempa, G. S. Jeon, K. Park, and Y. B. Kim, *Phys. Rev. Lett.* **109**, 066401 (2012).
- ¹⁹⁰ W. Witzczak-Krempa, A. Go, and Y. B. Kim, *Phys. Rev. B* **87**, 155101 (2013).
- ¹⁹¹ Y. Machida, S. Nakatsuji, Y. Maeno, T. Tayama, T. Sakakibara, and S. Onoda, *Phys. Rev. Lett.* **98**, 057203 (2007).
- ¹⁹² T. Kondo, M. Nakayama, R. Chen, J. J. Ishikawa, E.-G. Moon, T. Yamamoto, Y. Ota, W. Malaeb, H. Kanai, Y. Nakashima, Y. Ishida, R. Yoshida, H. Yamamoto, M. Matsunami, S. Kimura, N. Inami, K. Ono, H. Kumigashira, S. Nakatsuji, L. Balents, and S. Shin, *Nature Communications* **6**, 10042 (2015).
- ¹⁹³ E.-G. Moon, C. Xu, Y. B. Kim, and L. Balents, *Phys. Rev. Lett.* **111**, 206401 (2013).
- ¹⁹⁴ S. Nakatsuji, Y. Machida, Y. Maeno, T. Tayama, T. Sakakibara, J. v. Duijn, L. Balicas, J. N. Millican, R. T. Macaluso, and J. Y. Chan, *Phys. Rev. Lett.* **96**, 087204 (2006).
- ¹⁹⁵ Y. Machida, S. Nakatsuji, S. Onoda, T. Tayama, and T. Sakakibara, *Nature* **463**, 210 (2010).
- ¹⁹⁶ K. Ueda, J. Fujioka, Y. Takahashi, T. Suzuki, S. Ishiwata, Y. Taguchi, and Y. Tokura, *Phys. Rev. Lett.* **109**, 136402 (2012).
- ¹⁹⁷ M. Nakayama, T. Kondo, Z. Tian, J. J. Ishikawa, M. Halim, C. Bareille, W. Malaeb, K. Kuroda, T. Tomita, S. Ideta, K. Tanaka, M. Matsunami, S. Kimura, N. Inami, K. Ono, H. Kumigashira, L. Balents, S. Nakatsuji, and S. Shin, *Phys. Rev. Lett.* **117**, 056403 (2016).
- ¹⁹⁸ M. Sakata, T. Kagayama, K. Shimizu, K. Matsuhiro, S. Takagi, M. Wakeshima, and Y. Hinatsu, *Phys. Rev. B* **83**, 041102 (2011).
- ¹⁹⁹ F. F. Tafti, J. J. Ishikawa, A. McCollam, S. Nakatsuji, and S. R. Julian, *Phys. Rev. B* **85**, 205104 (2012).
- ²⁰⁰ K. Ueda, J. Fujioka, B.-J. Yang, J. Shiogai, A. Tsukazaki, S. Nakamura, S. Awaji, N. Nagaosa, and Y. Tokura, *Phys. Rev. Lett.* **115**, 056402 (2015).
- ²⁰¹ Z. Tian, Y. Kohama, T. Tomita, H. Ishizuka, T. H. Hsieh, J. J. Ishikawa, K. Kindo, L. Balents, and S. Nakatsuji, *Nature Physics* **12**, 134 (2016).
- ²⁰² K. Ueda, T. Oh, B.-J. Yang, R. Kaneko, J. Fujioka, N. Nagaosa, and Y. Tokura, *Nature Communications* **8**, 15515 (2017).
- ²⁰³ K.-Y. Yang, Y.-M. Lu, and Y. Ran, *Phys. Rev. B* **84**, 075129 (2011).
- ²⁰⁴ B.-J. Yang and N. Nagaosa, *Phys. Rev. Lett.* **112**, 246402 (2014).
- ²⁰⁵ T. Ohtsuki, Z. Tian, A. Endo, M. Halim, S. Katsumoto, Y. Kohama, K. Kindo, M. Lippmaa, and S. Nakatsuji, *Proceedings of the National Academy of Sciences* **116**, 8803 (2019).
- ²⁰⁶ T. C. Fujita, Y. Kozuka, M. Uchida, A. Tsukazaki, T. Arima, and M. Kawasaki, *Scientific Reports* **5**, 9711 (2015).
- ²⁰⁷ W. J. Kim, J. H. Gruenewald, T. Oh, S. Cheon, B. Kim, O. B. Korneta, H. Cho, D. Lee, Y. Kim, M. Kim, J.-G. Park, B.-J. Yang, A. Seo, and T. W. Noh, *Phys. Rev. B* **98**, 125103 (2018).
- ²⁰⁸ T. Takayama, A. Yaresko, A. Matsumoto, J. Nuss, K. Ishii, M. Yoshida, J. Mizuki, and H. Takagi, *Scientific Reports* **4**, 6818 (2014).
- ²⁰⁹ T. Takayama, A. N. Yaresko, A. S. Gibbs, K. Ishii, D. Kukusta, and H. Takagi, *Phys. Rev. Materials* **4**, 075002 (2020).
- ²¹⁰ L. S. I. Veiga, M. Etter, K. Glazyrin, F. Sun, C. A. Escanhoela, G. Fabbris, J. R. L. Mardegan, P. S. Malavi, Y. Deng, P. P. Stavropoulos, H.-Y. Kee, W. G. Yang, M. van Veenendaal, J. S. Schilling, T. Takayama, H. Takagi, and D. Haskel, *Phys. Rev. B* **96**, 140402 (2017).
- ²¹¹ T. Takayama, A. Krajewska, A. S. Gibbs, A. N. Yaresko, H. Ishii, H. Yamaoka, K. Ishii, N. Hiraoka, N. P. Funnell, C. L. Bull, and H. Takagi, *Phys. Rev. B* **99**, 125127 (2019).
- ²¹² V. Hermann, M. Altmeyer, J. Ebad-Allah, F. Freund, A. Jesche, A. A. Tsirlin, M. Hanfland, P. Gegenwart, I. I. Mazin, D. I. Khomskii, R. Valentí, and C. A. Kuntscher, *Phys. Rev. B* **97**, 020104 (2018).
- ²¹³ T. Biesner, S. Biswas, W. Li, Y. Saito, A. Pustogov, M. Altmeyer, A. U. B. Wolter, B. Büchner, M. Roslova, T. Doert, S. M. Winter, R. Valentí, and M. Dressel, *Phys. Rev. B* **97**, 220401 (2018).
- ²¹⁴ Z. Hiroi, J.-i. Yamaura, T. C. Kobayashi, Y. Matsubayashi, and D. Hirai, *Journal of the Physical Society of*

- Japan **87**, 024702 (2018).
- ²¹⁵ L. Fu, *Phys. Rev. Lett.* **115**, 026401 (2015).
- ²¹⁶ T. C. Lubensky and L. Radzihovsky, *Phys. Rev. E* **66**, 031704 (2002).
- ²¹⁷ V. Kozii and L. Fu, *Phys. Rev. Lett.* **115**, 207002 (2015).
- ²¹⁸ Y. Wang, G. Y. Cho, T. L. Hughes, and E. Fradkin, *Phys. Rev. B* **93**, 134512 (2016).
- ²¹⁹ J. W. Harter, Z. Y. Zhao, J.-Q. Yan, D. G. Mandrus, and D. Hsieh, *Science* **356**, 295 (2017).